The Cryosphere

Modeling seasonal-to-decadal ocean–cryosphere interactions along the Sabrina Coast, East Antarctica

Kazuya Kusahara[1], Daisuke Hirano[2,3], Masakazu Fujii[2,3], Alexander D. Fraser[4], Takeshi Tamura[2,3], Kohei Mizobata[5], Guy D. Williams[6], and Shigeru Aoki[7]

[1]Japan Agency for Marine-Earth Science and Technology (JAMSTEC), Yokohama, Kanagawa, 236-0001, Japan
[2]National Institute of Polar Research, Tachikawa, Tokyo, 190-8518, Japan
[3]Graduate University for Advanced Studies (SOKENDAI), Tachikawa, Tokyo, 190-8518, Japan
[4]Australian Antarctic Program Partnership, Institute for Marine and Antarctic Studies, University of Tasmania, nipaluna/Hobart, Tasmania, 7004, Australia
[5]Department of Ocean Sciences, Tokyo University of Marine Science and Technology, Tokyo, 108-8477, Japan
[6]Marine Solutions Tasmania, Newtown, Tasmania, 7008, Australia
[7]Institute of Low Temperature Science, Hokkaido University, Sapporo, Hokkaido, 060-0819, Japan

Correspondence: Kazuya Kusahara (kazuya.kusahara@gmail.com, kazuya.kusahara@jamstec.go.jp)

Abstract. The Totten Ice Shelf (TIS) and Moscow University Ice Shelf (MUIS), along the Sabrina Coast of Wilkes Land, are the floating seaward terminuses of the second-largest freshwater reservoir in the East Antarctic Ice Sheet. Being a marine ice sheet, it is vulnerable to the surrounding ocean conditions. Recent comprehensive oceanographic observations, including bathymetric measurements off the Sabrina Coast, have shed light on the widespread intrusion of warm modified Circumpolar Deep Water (mCDW) onto the continental shelf and the intense ice–ocean interaction beneath the TIS. However, the spatiotemporal coverage of the observation is very limited. Here, we use an ocean–sea ice–ice shelf model with updated bathymetry to better understand the regional ocean circulations and ocean–cryosphere interactions. The model successfully captured the widespread intrusions of mCDW, local sea ice production and the ocean heat and volume transports into the TIS cavity, facilitating an examination of the overturning ocean circulation within the ice shelf cavities and the resultant basal melting. We found notable differences in the temporal variability in ice shelf basal melting across the two adjacent ice shelves of the TIS and the western part of the MUIS. Ocean heat transport by mCDW controls the low-frequency interannual-to-decadal variability in ice–ocean interactions, but the sea ice production in the Dalton Polynya strongly modifies the signals, explaining the regional difference between the two ice shelves. The formation of a summertime eastward-flowing undercurrent beneath the westward-flowing Antarctic Slope Current is found to play an important role in the seasonal delivery of ocean heat to the continental shelf.

1 Introduction

Satellite-based observations have revealed that the Antarctic Ice Sheet has lost mass in recent decades (Rignot et al., 2019, 2008; Pritchard et al., 2012; Shepherd et al., 2018, 2012; Otosaka et al., 2022). This mass loss directly results in global sea level rise, with a far-reaching effect not only on the physical and biological environment of Earth, but also on human society (Mimura, 2013). The Intergovernmental Panel on Climate Change (IPCC) pointed out in the Sixth Assessment Report that the negative mass balance of the Antarctic Ice Sheet will become the major contributor to future sea level rise in the coming centuries, albeit with large uncertainties in the magnitude (IPCC, 2021). The Antarctic Ice Sheet gains mass by snow accumulation over the Antarctic continent and loses it mostly through two ablation processes at the surrounding ice shelves: basal melting at ice shelf bases and iceberg calving at ice shelf fronts (Greene et al., 2022). The total amount

of the Antarctic ice shelf basal melting has been estimated to be greater than that of iceberg calving (Rignot et al., 2013; Depoorter et al., 2013; Liu et al., 2015). Because the Antarctic ice shelf base is the place where the Southern Ocean directly interacts with the Antarctic Ice Sheet, oceanographic conditions along the Antarctic coastal margins are very important for understanding ice–ocean interactions linked to global sea level rise.

Regions of the Antarctic Ice Sheet where the bedrock is below sea level are called marine ice sheets. The bedrock of marine ice sheets in coastal regions tends to become deeper further inland. It is known that ice sheet and ice shelf systems on such retrograde slopes are more vulnerable to warm water intrusion into ice shelf cavities. This type of topography serves as a fundamental precondition for a phenomenon known as marine ice sheet instability (Weertman, 1974), causing grounding line retreat and eventually destabilizing the inner ice sheets. Note that multiple factors, including the retrograde slope, basal boundary conditions, ice sheet geometry, bed curvature, and ice–climate feedbacks, collectively contribute to the potential occurrence of the instability (Sergienko, 2022). In the present-day Antarctic Ice Sheet, marine ice sheets are found extensively in the West Antarctic Ice Sheet and in eastern parts of the East Antarctic Ice Sheet (the Aurora Subglacial Basin and the Wilkes Subglacial Basin), where rapid ice sheet mass loss by marine ice sheet instability could potentially occur (Morlighem et al., 2020; Fretwell et al., 2013). Many studies have focused on the West Antarctic Ice Sheet, and there is a growing consensus that intrusions of warm Circumpolar Deep Water (CDW) into continental shelf regions have eroded the West Antarctic ice shelves and grounding lines in recent decades (Payne et al., 2004; Shepherd et al., 2004; Kimura et al., 2017; Milillo et al., 2019; Naughten et al., 2022). Similar potentially unstable conditions have also recently been noted in the East Antarctic Ice Sheet due to improved bedrock topography (Fretwell et al., 2013; Morlighem et al., 2020) and advances in ice sheet modeling. One such area is the Totten Glacier (TG) in the Aurora Subglacial Basin, which has the seaward termination of the Totten Ice Shelf (TIS). Several ice sheet modeling studies of future and past warm periods have indicated that the mass loss from the ice sheet in the Aurora Subglacial Basin substantially contributes to global sea level rise as well as the mass loss from the West Antarctic Ice Sheet (Golledge et al., 2015; Pollard et al., 2015; DeConto and Pollard, 2016).

The TG is the second-largest freshwater reservoir in the East Antarctic Ice Sheet, storing ice that is equivalent to more than 3.5 m of the global sea level (Greenbaum et al., 2015; Li et al., 2015; Young et al., 2011; Morlighem et al., 2020). A substantial amount of ice is discharged from the glacier or ice sheet across the grounding line, estimated to be 69.0–72.6 Gt yr^{-1} for the period 1979–2017 (Rignot et al., 2019). The long-term mass balance of the TG over the period, estimated from a combination of satellite records and a regional

atmospheric climate model, has shown a cumulative mass loss of 236 Gt (Rignot et al., 2019). Several satellite observational studies over different analytical periods have reported a similar acceleration in the regional ice discharge (Li et al., 2016; Rignot et al., 2019). However, a recent study by Miles et al. (2022) showed a decreasing trend after the discharge peaked around 2010. The discrepancies between the conclusions of these studies are likely due to different periods and lengths of the analyses, indicating the presence of strong interannual variability and the need for long-term analysis to more robustly capture the changes. Variations in the ice velocity of the TG are tightly synchronized with changes in the glacier thickness and the grounding line position. An increase in the ice velocity or discharge is accompanied by thinning in the coastal area and grounding line retreat and vice versa (Li et al., 2015, 2016; Miles et al., 2022). Previous observational and modeling studies have inferred that the interannual variability in glaciers or ice sheets is strongly controlled by changes in surrounding ocean temperatures (Roberts et al., 2018; McCormack et al., 2021), in particular through the intrusion of warm modified CDW (mCDW) into the continental shelf region. A modeling study using an asynchronously coupled ice–ocean model to project future changes in the TG and TIS also suggested that an increase in mCDW in a warming climate will accelerate the mass loss and widespread retreat of the local grounding line (Sun et al., 2016; Pelle et al., 2021). Note that a recent study by Pelle et al. (2020) indicated, however, that the Totten Glacier may be less susceptible to marine ice sheet instability than previously thought, as the bedrock slope is prograde for approximately 10 km upstream of the current grounding line. However, this topographic configuration does not diminish the importance of changes in oceanic conditions for the glacier's sensitivity.

The coastal margin off the Sabrina Coast had few ocean observations until recently. Before an Australian oceanographic survey conducted in January 2015 (Rintoul et al., 2016; Silvano et al., 2017), there were only two CTD (conductivity, temperature, and depth) stations just south of the shelf break (Bindoff et al., 2000; Williams et al., 2011). Although these isolated CTD profiles showed the local presence of warm bottom-intensified mCDW on the continental shelf break, the details of their potential pathways across the shelf and the roles in ocean–cryosphere interaction were unclear at the time. Presenting ground-breaking new CTD and bathymetry data in front of the TIS, Rintoul et al. (2016) confirmed for the first time the direct access of warm mCDW toward the TIS through deep troughs. Silvano et al. (2017) used the extended oceanographic observations to show that mCDW is abundant in deep layers over the continental shelf region off the Sabrina Coast. The mCDW is transported from offshore across the shelf break (Hirano et al., 2021), and the locations of the intrusions are consistent with the southward flow of quasi-stationary cyclonic eddies formed over the continental slope and rise (Mizobata et al., 2020). While bathymetry plays a vital role in regulating oceanic transport

across the shelf break, over the continental shelf, and into ice shelf cavities, there is unfortunately a lack of precise regional bathymetry data in this area. Although recent oceanographic and geophysical studies have updated the available bathymetric data, the improvements have been somewhat piecemeal: Nitsche et al. (2017) detected wide and deep troughs within the shelf break, Silvano et al. (2019) pointed out a deeper depression in the continental shelf than the previous datasets had shown, and Greenbaum et al. (2015) derived ocean bathymetry under the TIS.

Several numerical modeling studies have been conducted to better understand basal melting at the TIS and the surrounding ocean (Gwyther et al., 2014, 2018; Khazendar et al., 2013; Nakayama et al., 2021; Van Achter et al., 2022). However, as mentioned above, there remain large uncertainties in the regional bathymetry. In addition, the selection of bathymetry in past modeling studies was largely left to the discretion of the modeler, e.g., the use of the most recent one available at the time, the modelers' preference, or constraints in their model configuration. Due to the bathymetric uncertainties, the previous studies could only focus on individual processes in the overall ocean–cryosphere system, such as mCDW intrusion, coastal water mass transformation in polynyas, or ice shelf basal melting at the TIS. While the previous modeling studies all determined the presence of warm mCDW inflow into the continental shelf region, there were varying representations of its spatial patterns. It has been suggested that the inflow of mCDW into continental shelf regions is related to the Antarctic Slope Front/Current (ASF/ASC) system in the upper continental slope region (Nakayama et al., 2021; Thompson et al., 2018; Silvano et al., 2019; Liu et al., 2022) and that sea ice production in local coastal polynyas plays a vital role in distinct water mass transformations over the continental shelf (Gwyther et al., 2014; Khazendar et al., 2013). It should be kept in mind that the results in these previous regional models were heavily influenced by their lateral boundaries, the conditions which were often derived from a different coarse-resolution ocean model. Furthermore, the model integration periods (10–20 years) used in many of the previous studies are too short to be used in a detailed examination of interannual variability.

In this context, a recent study by Hirano et al. (2023) comprehensively described the regional ocean circulation of mCDW from the shelf break to the TIS, using new bathymetry, extensive oceanographic observations over the Totten continental shelf, and results from a high-resolution ocean model. Our study uses the same model to conduct a detailed examination of the seasonal, interannual, and decadal variability, complementing the modeling part in Hirano et al. (2023), which used the annual-mean climatology. Together with the inclusion of the updated bathymetric data off the Sabrina Coast, the strengths of our numerical model include the novel model configuration whose entire model domain is the Southern Ocean with a horizontal resolution within the

focal region of less than 4 km (Fig. 1) and a long integration period over 70 years. These improvements allow us to represent regional ice–ocean interactions which were consistent with the recent observation (Hirano et al., 2023), and we can extend the discussion to longer interannual-to-decadal timescales. In Sect. 2, we describe the model configuration, including the model bathymetry. A detailed comparison with several existing bathymetric datasets can be found in the Appendix. We then show model results for the sea ice field (Sect. 3), the ice shelf basal melting (Sect. 4), the ocean fields over the continental shelf, the ocean circulation within the ice shelf cavities (Sect. 5), and the ocean–cryosphere linkage between them (Sect. 6).

2   Model configuration

2.1   An ocean–sea ice–ice shelf model

This study utilized an ocean–sea ice–ice shelf model (Kusahara and Hasumi, 2013, 2014) previously employed in both regional and circumpolar Southern Ocean modeling studies (e.g., Kusahara et al., 2017; Kusahara, 2021). The model equations are solved in an orthogonal, curvilinear, and horizontal coordinate system (Hasumi, 2006). The horizontal coordinate has two singular points, and we placed the model's singular points on the same longitude (75° S, 120° E and 0°, 120° E) to regionally increase the horizontal resolution off the Sabrina Coast (Fig. 1a) while maintaining a circumpolar Southern Ocean of the model's domain. With this configuration, the focal region can be covered with a horizontal resolution of less than 4 km, allowing us to reasonably resolve the bathymetry and coastal boundaries of the land, ice shelves, and fast ice (i.e., "icescape") in the model. An artificial northern solid boundary was placed in a latitude range of 43 to 30° S, varying with longitude. Although the horizontal resolution becomes coarser outside the region of interest, the model's grid configuration has a strong advantage in escaping the nontrivial issue of the east–west lateral boundary conditions of regional models in the Southern Ocean. Such methods have often been used in Antarctic coastal ocean modeling studies (Marsland et al., 2004; Kusahara et al., 2021). The ocean component uses the z-coordinate system with the following vertical grid spacing from the surface to the bottom: 4 levels of 5 m, 59 levels of 20 m, 30 levels of 40 m, and 31 levels of 100 m. Partial step representation is adopted for the bathymetry and ice shelf draft (Adcroft et al., 1997).

The sea ice and ice shelf components in the model are the same as those used in our previous study of regional ocean–cryosphere interactions in Lützow-Holm Bay (Kusahara et al., 2021). There are landfast-ice-covered regions along the Sabrina Coast, which characterizes the regional icescape (Fraser et al., 2012, 2021; Van Achter et al., 2022; Nihashi and Ohshima, 2015). It is important to take account of the landfast-ice distribution for reproducing sea ice pro-
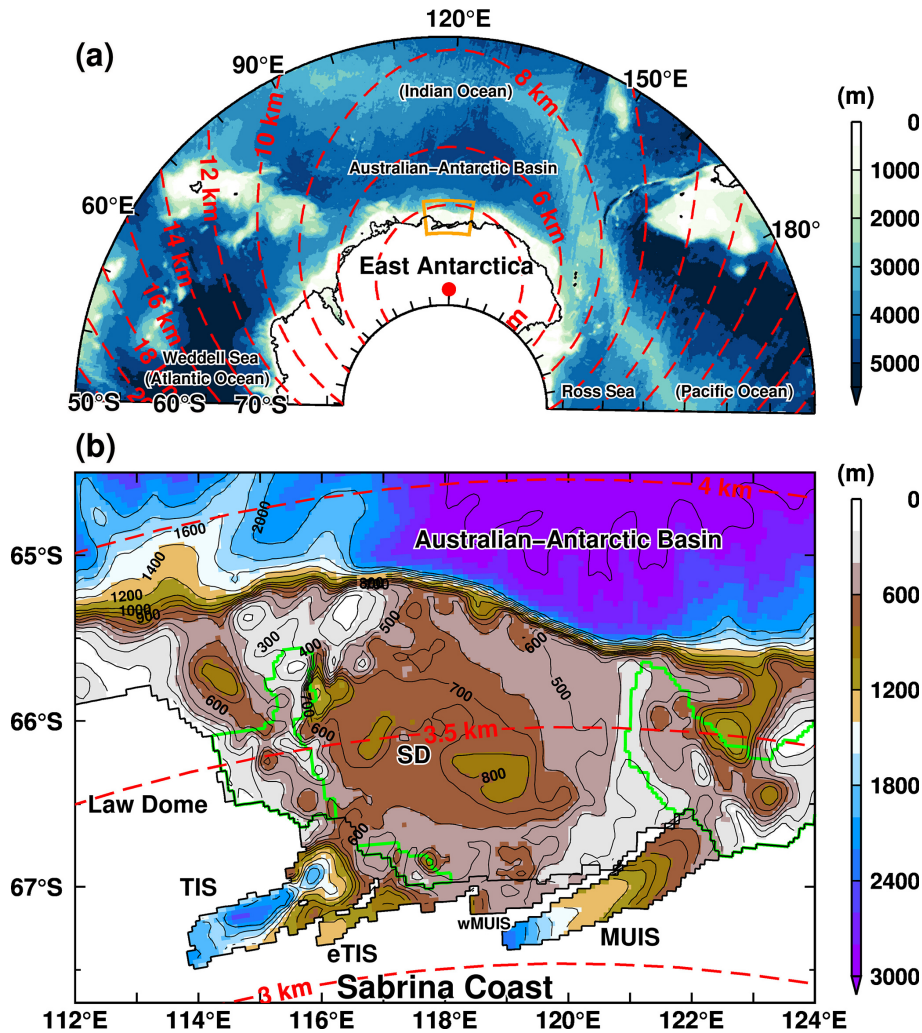
Figure 1. Model bathymetry (background colors) and horizontal resolution (red dashed contours) over **(a)** East Antarctica and **(b)** the region off the Sabrina Coast. The red dot in panel **(a)** represents one of the model's singular points. The orange box in panel **(a)** shows the region for panel **(b)**. The major place names shown in panel **(a)** are as follows: the Weddell Sea in the Atlantic Ocean, the Australian Antarctic Basin in the Indian Ocean, and the Ross Sea in the Pacific Ocean. In panel **(b)**, TIS, eTIS, wMUIS, MUIS, and SD represent the Totten Ice Shelf, the eastern Totten Ice Shelf, the western Moscow University Ice Shelf, the Moscow University Ice Shelf, and the Sabrina Depression, respectively. The depth contour intervals are 100, 200, and 1000 m for regions shallower than 1000 and 1000–2000 m and deeper than 2000 m, respectively. The black zigzag lines represent grounding and ice front lines, and the green line indicates the fast ice edge.

duction in the model. In this study, observation-based areas of persistent landfast-ice cover (Fraser et al., 2012) were specified as thin ice shelf grid cells with a constant thickness (5 m). As a first approximation, the spatial distribution of landfast ice was assumed to be constant throughout the model integration. We used observation-based coefficients of the thermal and salinity exchange velocities for the ice shelf ($\gamma_t = 1.0 \times 10^{-4}\,\mathrm{m\,s^{-1}}$, $\gamma_s = 5.05 \times 10^{-7}\,\mathrm{m\,s^{-1}}$, Hellmer and Olbers, 1989) and applied one-tenth coefficients for landfast ice to consider the difference in the tidal speed between the ice shelf cavity and the open ocean in the parameterization. In our previous ocean modeling for Lützow-Holm Bay, we confirmed that the magnitude of landfast-ice melting did not

significantly affect the variability in the inflow of mCDW onto the continental shelf (Kusahara et al., 2021). Regarding the ice–ocean parameterization, it is worth noting that many ice shelf–ocean modeling studies utilized velocity-dependent coefficients for solving ice–ocean interactions (Holland and Jenkins, 1999; Malyarenko et al., 2020). Given that the magnitude of ocean velocity under ice shelves can be strongly influenced by various factors, including both horizontal and vertical grid resolutions (Gwyther et al., 2020) as well as unmodeled processes like tidal effects and submesoscale eddy activities, we opted for the velocity-independent scheme of Hellmer and Olbers (1989) that assumed a constant ocean velocity of 15 cm s^{-1}. It should be noted that using the velocity-

independent parameterization also implies that we ignore the local enhancement in melt rates due to the formation of buoyant upslope plumes arising from the upstream ice shelf melting. However, such effects are considered secondary compared to the primary influence of the dominant heat supply through warm water inflow into the ice shelf cavities.

2.2 Bathymetry off the Sabrina Coast

Previous ocean modeling studies of Antarctic coastal regions (Kusahara et al., 2021; Sun et al., 2022) have pointed out a general concern about the accuracy of bathymetry along the Antarctic coastal region, where bathymetric data are not well constrained due to the insufficient number of direct water depth observations. This is especially true for the region off the Sabrina Coast. Severe sea ice conditions and a large area of permanent or multiyear landfast ice restricts access to these areas, which limits direct observations. As shown in the Appendix, there are considerable differences between the regional bathymetry in the available datasets (Fig. A1), which reflects the large uncertainty. A recent observational study by Hirano et al. (2023) was successful in measuring key bathymetric features using a multibeam echo sounder and airborne-based expendable sensors (Fig. A1a), and they compiled a regional bathymetry, blending their observations with GEBCO2020 (Fig. A1b). Figure A1c–f show horizontal maps of the bathymetry off the Sabrina Coast in four different datasets: GEBCO2020 (GEBCO_2020 Grid, 2020), BedMachine Antarctica v2 (Morlighem et al., 2020), RTopo-2 (Schaffer et al., 2016), and ETOPO1 (Amante and Eakins, 2009).

2.3 Atmospheric conditions

The ocean–sea ice–ice shelf model was forced with atmospheric surface boundary conditions that include wind stresses, wind speed, air temperature, specific humidity, downwelling shortwave radiation, downwelling longwave radiation, sea level air pressure, and freshwater flux. In this study, the daily surface boundary conditions were estimated from ERA5 datasets (Hersbach et al., 2020; Bell et al., 2021) using the bulk formula of Kara et al. (2000) for wind stresses and sensible and latent heat fluxes.

To understand atmospheric forcing, we calculated the seasonal climatology of sea level pressure and surface wind averaged from 1981 to 2010 (Fig. 2). There are three low-pressure systems over the Southern Ocean, and the Sabrina Coast is located on the southeastern side of the low-pressure system in the Indian sector (see the red box in Fig. 2). Westerly and easterly winds prevail throughout the year to the north (equatorward of $63°$ S) and south (poleward of $64°$ S), respectively, of this low-pressure system. Note that the wind regime (negative wind stress curl) creates the Antarctic divergence zone where deep CDW can dynamically move upward to the subsurface due to surface Ekman divergence

(Marshall and Speer, 2012; Tamsitt et al., 2017). In addition, the prevailing easterly wind in the coastal region is the driver of westward-flowing ocean currents along the Antarctic coastal regions known as the ASF/ASC system (Thompson et al., 2018). The wind off the Sabrina Coast is directed west-northwest throughout the year and reaches a maximum ($> 5.5\,\mathrm{m\,s^{-1}}$) in the fall and winter seasons (from June to August), which is consistent with the seasonal cycle of local atmospheric pressure. The wind speed in the spring and summer seasons is relatively low, but the magnitude is larger than $3.0\,\mathrm{m\,s^{-1}}$ in the climatology.

2.4 Boundary and initial conditions and spin-up integration

The model's initial oceanic properties of temperature and salinity were derived from January fields in the World Ocean Atlas 2018 (Locarnini et al., 2018; Zweng et al., 2019), and the velocity fields were filled with zero over the model domain. For the water properties in the ice shelf cavities, ocean properties at the nearest oceanic grid were used. North of $40°$ S or near the artificial northern wall, the water properties were restored to the monthly climatology with a damping timescale of 10 d. In the region where the horizontal resolution is coarser than 4.2 km, the sea surface salinity (SSS) was restored to the monthly climatology to avoid unrealistically deep convection. There is no SSS restoring in the focal region. We ran the ocean–sea ice–ice shelf model for 30 years with 1951–1960 forcing (e.g., three cycles) and subsequently performed a 3-year adjustment with the 1951 forcing to obtain a spun-up initial condition for use in the historical experiment for the period 1951–2021 (the "CTRL" case).

To monitor the spinup of the ocean–cryosphere system off the Sabrina Coast, we use the time series of the total ice shelf basal melt amount in the region as the sum of the TIS, eTIS, wMUIS, and MUIS (Fig. S1 in the Supplement). This is a useful metric because the basal melting is controlled by the integrated effects from the interactions across local sea ice processes, the large and regional ocean circulation, and coastal water mass formation. At the beginning of the first cycle, ice shelf basal melting is very active, with a melting amount larger than $200\,\mathrm{Gt\,yr^{-1}}$, but it decreases to $50\,\mathrm{Gt\,yr^{-1}}$ within approximately 5 years. In the second half of the first cycle, ice shelf basal melting varies between 50 and $100\,\mathrm{Gt\,yr^{-1}}$. Active melting at the beginning is due to the extrapolation of relatively warm water from the nearest ocean grids to ice shelf cavities. A comparison of ice shelf basal melting between the three cycles demonstrates that the model reaches quasi-steady conditions in ice shelf basal melting and the relevant coastal processes after the long 30-year spinup integration. As shown later, 1951 is a relatively cold year, and sea ice production is accordingly high. In the 3-year adjustment with the 1951 forcing, the ocean conditions are adjusted to cold conditions (purple line in Fig. S1). Comparing ice shelf melting in the spinup experiments (second and third
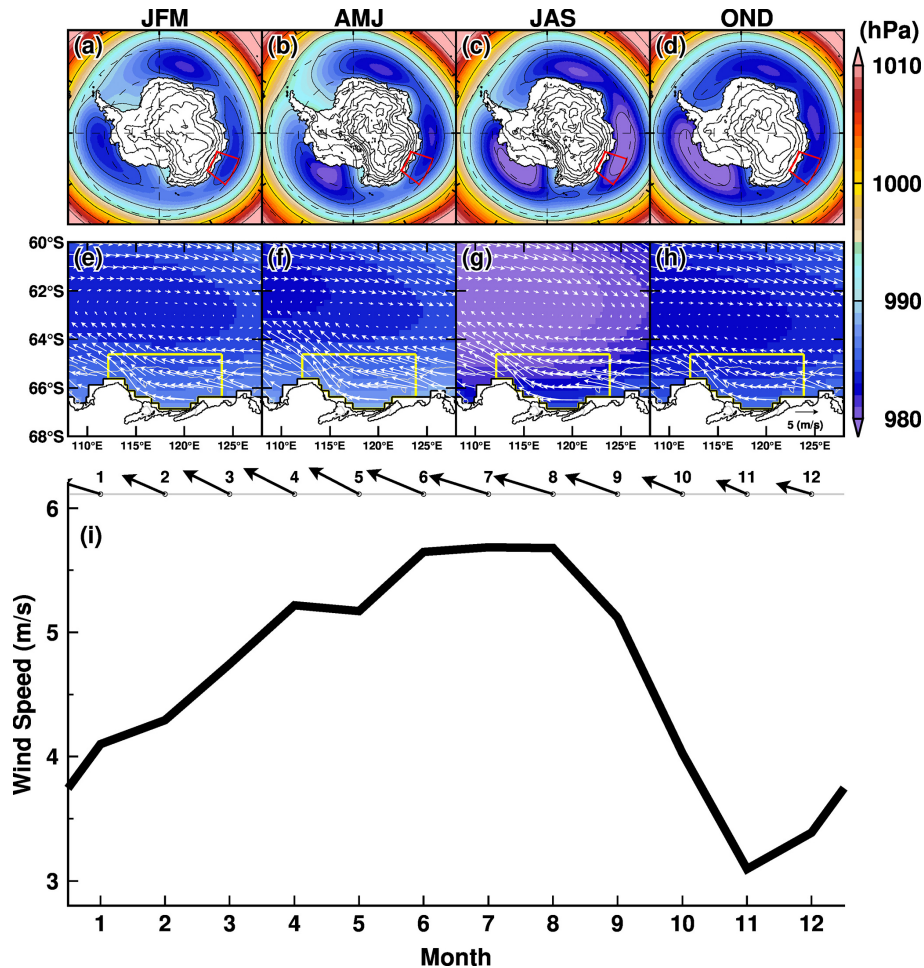
Figure 2. Seasonal climatology of atmospheric sea level pressure **(a–d)** over the Southern Ocean and **(e, f)** in the region off the Sabrina Coast (108–128° E). Color and vectors show the 3-month averages of atmospheric sea level pressure and wind, respectively. The climatology fields were calculated from the ERA5 dataset for the reference period 1981–2010. The red boxes in panels **(a–d)** indicate the region for panels **(e–h)**; the yellow boxes in panels **(e–h)** are the areas used to average the 10 m wind for panel **(i)**. In panel **(i)**, the monthly climatologies of wind vectors and wind speeds are shown.

cycles and 3-year adjustment) with the CTRL case, the differences are evident in the first 2 years, but the subsequent interannual variability is similar among them.

We performed an additional experiment in which the model continued to be forced with the 1951 surface forcing to check for inherent model drift ("CKDRF" case). The integration period is 1951–2021. In this paper, we do not mention the results from the CKDRF case, but the results are shown in the figures to confirm that the results from the CTRL case are not model drift.

3   Sea ice extent and production

Sea ice strongly characterizes the ocean surface conditions over the Southern Ocean. The presence or absence of sea ice and the formation or melting processes play a vital role in regulating ocean surface exchanges of heat, salt, freshwa-

ter, and momentum between the atmosphere and the ocean. Therefore, it is essential for this study to assess the reproducibility of sea ice fields in the model before delving into the ice–ocean interaction. Here, we show the model's sea ice representation, paying attention to the large-scale sea ice extent and coastal sea ice production off the Sabrina Coast. In particular, the coastal sea ice production significantly impacts the temporal variations in coastal ocean conditions and ice shelf basal melting, as shown in the later sections.

Figure S2 in the Supplement shows the observed and modeled seasonal cycles of regional sea ice concentration and extent from 108 to 128° E. We used the observed sea ice concentration derived from satellite passive microwave data using the NASA team algorithm (Cavalieri et al., 1984; Swift and Cavalieri, 1985). The monthly and seasonal averages were calculated from 1981 to 2010. Although sea ice extent in the model tends to be underestimated throughout the

year (Fig. S2i), the model reproduces seasonal changes in the spatial pattern of sea ice concentration, capturing a large-scale east–west gradient and small-scale features controlled by the coast and ice front line (Fig. S2a–h). Looking at the coastal regions, the model successfully represents the Dalton Polynya on the western side of the prolonged landfast ice at approximately $122°$ E and the year-round high sea ice concentration just north of the TIS. We calculated the regional sea ice extent anomaly, defined as the monthly deviation from the monthly climatology for the reference period (1981–2010), to assess the interannual variation in the model (Fig. S3 in the Supplement). In all the months, there are significant correlations between the observations and the model. Particularly in the colder months from April to October, the correlations are higher than 0.8. This indicates that the model reasonably represents interannual variation as well as the seasonal cycle, providing us with the confidence to examine further seasonal-to-interannual interactions between the sea ice and the upper ocean.

Sea ice production is an essential metric for the formation and transformation of Antarctic coastal water masses (Morales Maqueda et al., 2004). Sea ice forms during cold months when large amounts of heat are lost from the ocean due to intensive cooling by the atmosphere. Since sea ice can contain less salt than the ocean, excess salt is released into the ocean surface during sea ice formation (e.g., brine rejection). It should be noted that the sea ice salinity in the model is assumed to be 5 psu. When sea ice forms, cold (surface freezing point), high-salinity, and dense water is formed, causing an unstable ocean condition and subsequent local convection. The Dalton Polynya is formed over the eastern part of the Sabrina Depression (Tamura et al., 2008; Nihashi and Ohshima, 2015; Orsi and Webb, 2022). Figure 3 shows the horizontal distribution of annual sea ice production in the model, representing the Dalton Polynya with high sea ice production (up to $10 \, \mathrm{m \, yr^{-1}}$). The southern and western parts of the Sabrina Depression show relatively low sea ice production ($< 3 \, \mathrm{m \, yr^{-1}}$). The east–west contrast of sea ice production in this region is roughly consistent with the distribution described by satellite-based estimations (Tamura et al., 2008, 2016; Nihashi and Ohshima, 2015; Nakata et al., 2021). The seasonal variation indicates active sea ice production from March to October, with a peak from May to July (Fig. 3b).

The mean sea ice production over the Sabrina Depression (SD box in Fig. 3a) for the reference period (1981–2010) is $98.3 \, \mathrm{km^3 \, yr^{-1}}$ with a standard deviation of $12.6 \, \mathrm{km^3 \, yr^{-1}}$. The modeled sea ice production fluctuates between 80 and $120 \, \mathrm{km^3 \, yr^{-1}}$ from 1951 to 2021 (Fig. 3c). The sea ice production in the Dalton Polynya estimated from surface heat flux calculation ranges from 35 to $51 \, \mathrm{km^3 \, yr^{-1}}$ (Tamura et al., 2008, 2016; Nihashi and Ohshima, 2015; Nakata et al., 2021), while that estimated from sea ice divergence is around $197 \, \mathrm{km^3 \, yr^{-1}}$ (Orsi and Webb, 2022). Although there is a wide range in the observations, the sea ice production reproduced in the model is within the range of these estimates (Ta-

Table 1. Comparison of sea ice production off the Sabrina Coast with previous studies.

	Sea ice production ($\mathrm{km^3 \, yr^{-1}}$)	Period
This study	98.3 ± 12.6	1981–2010
	1006 ± 13.1	1951–2021
Tamura et al. (2008)	42.6 ± 6.7	1992–2001
Nihashi and Ohshima (2015)	35 ± 4	2003–2010
Tamura et al. (2016)	51 ± 10	1992–2013
Nakata et al. (2021)	42 ± 4	2003–2010
Orsi and Webb (2022)	197.4	2003–2015

ble 1), demonstrating that the model reasonably represents the surface forcing through the coastal sea ice formation. It should be noted that since the observational estimates from the heat flux calculation were only conducted in thin sea ice areas, the total sea ice production estimates tend to be smaller than those for the region over the Sabrina Depression.

4 Ice shelf basal melting

The model represents intensive ice–ocean interaction at the base of the ice shelves along the Sabrina Coast (Fig. 4 and Table 2). In this study, we mainly use the climatology of the ice shelf basal melt amount and rate averaged over the reference period (1981–2010) to examine the magnitude and spatial distribution. While the main conclusion remains the same independent of the averaging periods, this period was chosen to coincide with the reference period for the sea ice analysis and to examine the long-term mean field to minimize the influence of interannual variations. For our convenience, the ice shelves were categorized into four groups from west to east based on their geographic location: TIS, eTIS (eastern TIS), wMUIS (western MUIS), and MUIS. High melting rates exceeding $10 \, \mathrm{m \, yr^{-1}}$ are found near the grounding line of all the ice shelves (Fig. 4a). In particular, melt rates of $15 \, \mathrm{m \, yr^{-1}}$ or higher are reproduced over a wide area near the TIS grounding line zone, indicating very intense ice shelf basal melting. It should be noted that the satellite-based observation estimates for circumpolar mean Antarctic ice shelf basal melt rates are around $0.81 \pm 0.11 \, \mathrm{m \, yr^{-1}}$ (Depoorter et al., 2013) to $0.85 \pm 0.1 \, \mathrm{m \, yr^{-1}}$ (Rignot et al., 2013), which are much smaller than the regional melt rate modeled here.

Here we summarize the regional ice shelf basal melt amount and rate in the model (Table 2a) and compare them to the satellite-based estimates (Table 2b, Adusumilli et al., 2020; Depoorter et al., 2013; Liu et al., 2015; Rignot et al., 2013). Table 2a shows the values for two periods of the reference period (1981–2010) and the entire period of the model integration (1951–2021). In the model, the TIS has the highest ice shelf basal melt rate of approximately $8 \, \mathrm{m \, yr^{-1}}$, followed by the eTIS melt rate of approximately $6 \, \mathrm{m \, yr^{-1}}$. The
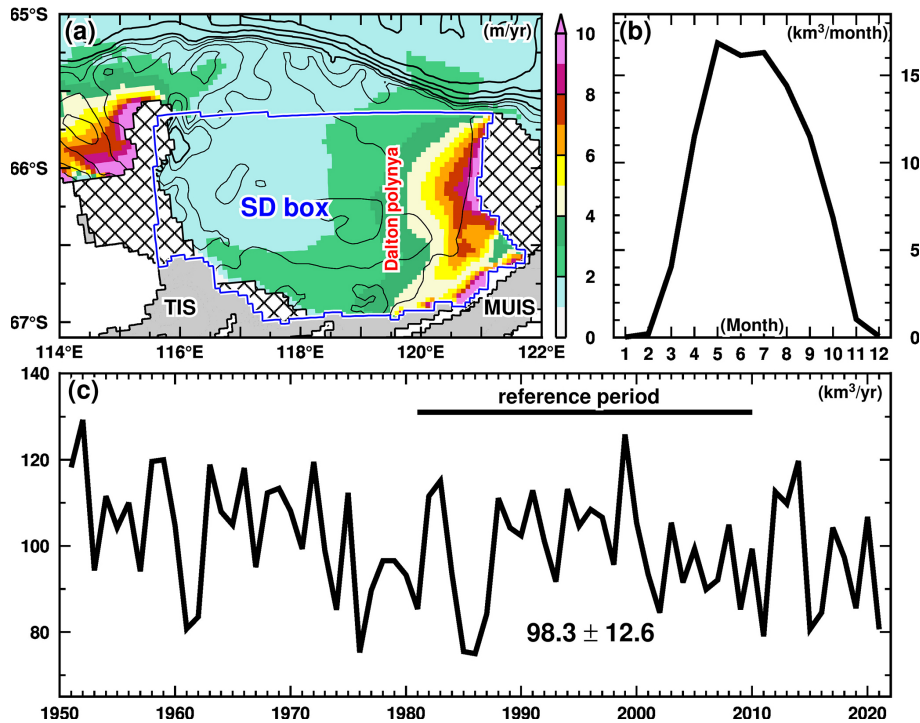
Figure 3. Modeled sea ice production. **(a)** Annual sea ice production map, **(b)** monthly sea ice production over the Sabrina Depression (SD) box, and **(c)** the interannual variability. The annual and monthly sea ice production in panels **(a)** and **(b)** is obtained from the climatology of the reference period (1981–2010).

ice shelf basal melt rate at the wMUIS is lower than $5\,\mathrm{m\,yr^{-1}}$, and that of the MUIS is larger than $5.6\,\mathrm{m\,yr^{-1}}$. The modeled ice shelf basal melting amounts over the whole TIS (TIS + eTIS) and the whole MUIS (wMUIS + MUIS) are estimated to be approximately 48–51 and 27–$28\,\mathrm{Gt\,yr^{-1}}$, respectively. The modeled ice shelf basal melting amount and rate for the whole TIS are slightly smaller than the observational estimates, which range from 59 to $64\,\mathrm{Gt\,yr^{-1}}$, while those for the whole MUIS are very comparable to the observational estimates: 26–$28\,\mathrm{Gt\,yr^{-1}}$. A recent estimate of the ice shelf basal rate near the TIS grounding line by an autonomous phase-sensitive radio-echo sounder (ApRES) was $22\,\mathrm{m\,yr^{-1}}$, which was reported to be lower by about 40 % than the satellite observations (Vaňková et al., 2021). The model shows ice shelf basal melting at a rate higher than $20\,\mathrm{m\,yr^{-1}}$ at the grounding line (Fig. 4a), which is consistent with the ApRES estimate. Although both the model and satellite observations have their own biases in ice shelf basal melting, we consider the model to adequately reproduce the active ice shelf basal melting along the Sabrina Coast.

Next, we show the amplitudes and months of the maximum and minimum to examine the seasonal cycle of the ice shelf basal melt rate (Fig. 4b–d). The amplitude was defined as the difference in the basal melt rate between the maximum and minimum months. The seasonal amplitude is smaller than the annual-mean ice shelf basal melt rate, indicating active ice–ocean interaction throughout the year. The southern

halves of the TIS and MUIS and the entire wMUIS have a relatively strong seasonality with an amplitude higher than $4\,\mathrm{m\,yr^{-1}}$, whereas the northern halves of the TIS and MUIS exhibit a moderate seasonality. The wMUIS and MUIS ice shelves have maxima from February to March and minima from July to October. The seasonal amplitude of the ice shelf melt rate over the TIS is widely heterogeneous from region to region, as also confirmed in seasonal variations in the ice shelf melt rate averaged every 25 km from the ice front (Fig. S4 in the Supplement). In the region within 25 km of the ice front, there is a minor seasonal variation. In the 25–50 km region, the minimum is in April and the maximum is in July–August. In the 50–75 km region, the minimum is in April and the maximum is in September–October. Near the groundling zone, the minimum is in May and the maximum is in September–October. These results indicate the increased seasonal amplitude and delayed seasonality with distance from the ice front.

The time series of the modeled basal melting amount at the four ice shelves are shown in Fig. 5 (blue and red lines for the monthly and annual averages, respectively). The time series in the CTRL case substantially deviated from that in the CKDRF case, confirming that the interannual variability in the CTRL case is not due to artificial drift or inherent model variability. The temporal variability at the TIS/eTIS and wMUIS/MUIS differs considerably, with low-frequency interannual-to-decadal variability predominating in the TIS
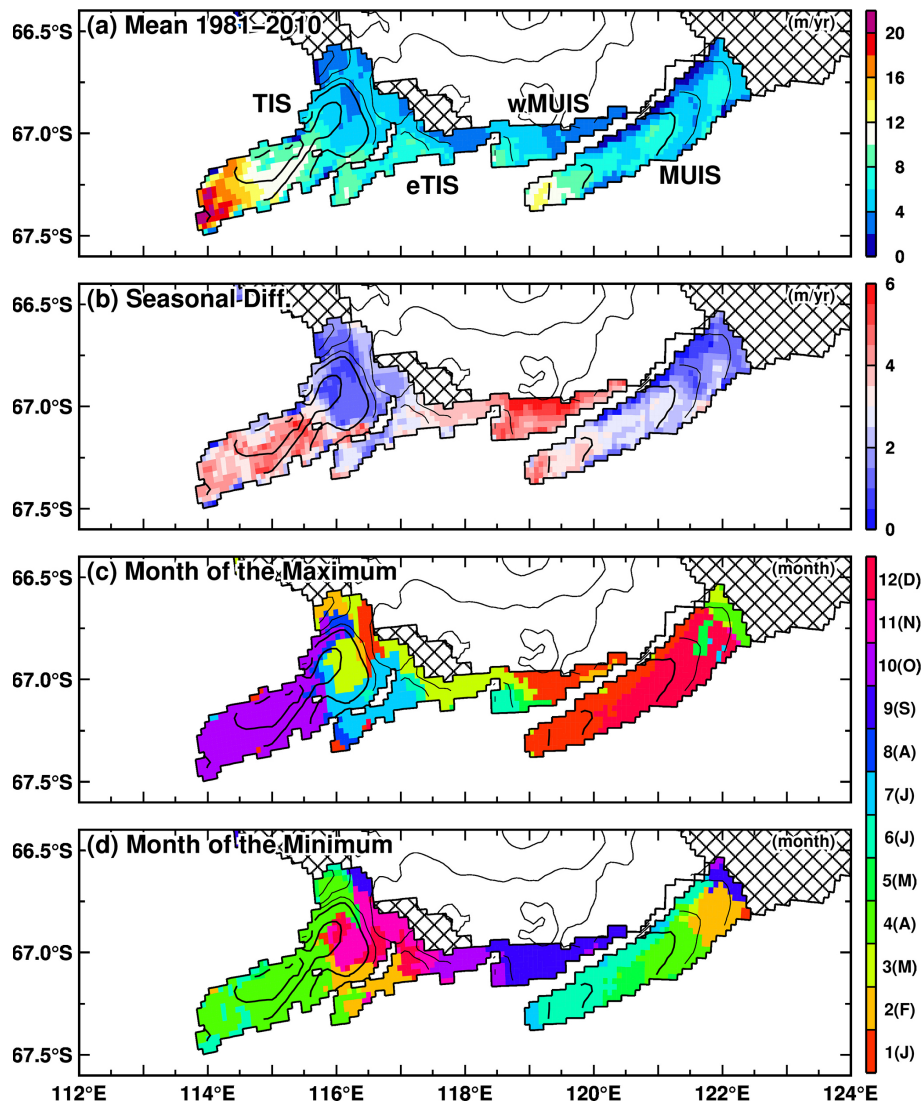
Figure 4. Maps of the **(a)** annual mean ice shelf basal melt rate, **(b)** seasonal amplitude, and **(c, d)** months of the maximum and minimum. The climatology averaged over the reference period 1981–2010 is used for the plots.

regions and high-frequency seasonal variability dominating in the MUIS regions. Wavelet power spectra (Torrence and Compo, 1998) for the modeled ice shelf basal melting amount were calculated to quantify the differences in the temporal variability (Fig. S5 in the Supplement). It should be noted that the power spectrum was normalized by variance to compare different time series with different magnitudes of variability and was also divided by scales to rectify the wavelet power spectrum (Liu et al., 2007). The normalized power spectrum is displayed in logarithmic form in Fig. S5, and thus positive values indicate where the variation is higher than 1 standard deviation. There is seasonal variation in the TIS basal melting, but it is not statistically significant for many years. Considerable variability is found in the 2–11-year period band, with intermittent statistically significant variability at around 8 years for the period 1960–2000.

The general pattern of the power spectrum in the frequency–time domain of the ice shelf basal melting at the wMUIS is similar to that of the TIS but with a statistically significant 1-year signal and nonsignificant interannual variability. These results indicate that the ice shelves are subject to common low-frequency forcing and localized high-frequency forcing.

5 Ocean properties, currents, and transports

The thickness of the ice shelves along the Sabrina Coast ranges from tens of meters to a few hundred meters at the ice shelf's edge to several hundred meters to over 1000 m towards the grounding line. The ice shelf is a thermal insulator between the ocean and the atmosphere, and the lateral flow of warm (relative to the depth-dependent freezing point)

Table 2. (a) Annual mean ice shelf basal melt rate ($\mathrm{m\,yr^{-1}}$) and amount ($\mathrm{Gt\,yr^{-1}}$) for two periods (1981–2010 and 1951–2021). TIS indicates the Totten Ice Shelf, MUIS the Moscow University Ice Shelf, eTIS the eastern TIS, and wMUIS the western MUIS. **(b)** Observation-based annual mean basal melt rate ($\mathrm{m\,yr^{-1}}$) and amount ($\mathrm{Gt\,yr^{-1}}$) of the total TIS and the total MUIS.

(a)

Ice shelf	Area ($\mathrm{km^2}$)	1981–2010		1951–2021	
		Amount ($\mathrm{Gt\,yr^{-1}}$)	Rate ($\mathrm{m\,yr^{-1}}$)	Amount ($\mathrm{Gt\,yr^{-1}}$)	Rate ($\mathrm{m\,yr^{-1}}$)
TIS	5581	41.7 ± 5.8	8.1 ± 1.1	38.9 ± 7.8	7.6 ± 1.5
eTIS	1651	9.1 ± 1.3	6.0 ± 0.9	8.7 ± 1.6	5.8 ± 1.0
Total TIS	7232	50.8 ± 7.0	7.7 ± 1.1	47.7 ± 9.3	7.2 ± 1.4
wMUIS	1295	5.7 ± 1.1	4.8 ± 0.9	5.5 ± 1.2	4.7 ± 1.0
MUIS	4219	22.2 ± 2.7	5.7 ± 0.7	21.8 ± 9.3	5.6 ± 0.7
Total MUIS	5514	27.9 ± 3.6	5.5 ± 0.7	27.3 ± 3.7	5.4 ± 0.7

(b)

Total TIS	Amount ($\mathrm{Gt\,yr^{-1}}$)	Rate ($\mathrm{m\,yr^{-1}}$)	Period
Rignot et al. (2013)	63.2 ± 4	10.5 ± 0.7	2007–2008
Depoorter et al. (2013)	64 ± 12	9.89 ± 1.92	2007–2009
Liu et al. (2015)	63 ± 5	14.1 ± 1.2	2005–2011
Adusumilli et al. (2020)	64.0 ± 11.0	11.5 ± 2.0	1994–2018
	59.4 ± 11.0	NA	2010–2018

Total MUIS	Amount ($\mathrm{Gt\,yr^{-1}}$)	Rate ($\mathrm{m\,yr^{-1}}$)	Period
Rignot et al. (2013)	27.4 ± 4	4.7 ± 0.8	2007–2008
Depoorter et al. (2013)	28 ± 7	4.93 ± 1.32	2007–2009
Liu et al. (2015)	26 ± 3	6.4 ± 0.7	2005–2011
Adusumilli et al. (2020)	28.3 ± 8.0	7.4 ± 2.1	1994–2018
	25.8 ± 8.0	NA	2010–2018

NA: not available

ocean water into the ice shelf cavities is the main cause of ice shelf basal melting. The inflow is linked to both the local water mass transformation and the regional ocean circulations over the continental shelf and slope regions. In this section, in order to understand the regional ocean–cryosphere interactions along the Sabrina Coast, we present vertical and spatial distributions of ocean properties and velocity and calculate ocean volume and heat transport across some key sections. The model results are presented in the following order: near the ice front and under ice shelves (Sect. 5.1), over the Sabrina Depression (Sect. 5.2), and around the shelf break and upper continental slope region (Sect. 5.3).

5.1 Ice front region and under the ice shelf

To begin with, we show vertical profiles of ocean temperature, salinity, and velocity along a section 5 km offshore from the Antarctic coast and ice front (Fig. 6). This figure shows the annual-mean fields averaged over the reference period. Signals of warm, high-salinity, and relatively dense water are identified in deep troughs in front of the ice shelves. As shown later, this warm deep water near the coastline and ice shelf front originates from intrusions of mCDW

onto the continental shelf across the shelf break. Along this section, the mCDW signal is clearly seen in the density layers denser than $27.6\,\mathrm{kg\,m^{-3}}$. The velocity field shows clearly that mCDW is trapped in the deep troughs, and warm deep water flows toward the ice shelf cavities, with velocity magnitudes above $5\,\mathrm{cm\,s^{-1}}$. The warm deepwater signals are separated by a shallow bank located zonally between 119.5 and $122°\,\mathrm{E}$, indicating less water exchange in the denser layers. Compensating flows are found in the upper layers lighter than $27.6\,\mathrm{kg\,m^{-3}}$, reflecting a part of the typical ocean circulation formed in ice shelf cavities.

Next, we examine seasonal variations in volume and heat transports (referenced to $-2.0°\mathrm{C}$) into each ice shelf cavity across the ice shelf fronts (Fig. 7). We used the monthly mean outputs of the ocean water properties and velocities for this calculation. The volume transports and the mean temperatures were calculated for each $0.02\,\mathrm{kg\,m^{-3}}$ bin of the potential density for the inflow and outflow components. Net inflow transport was determined only when the difference between inflow and outflow transport was positive. Figure 7a–d show the net inflow volume transports in each density bin and the mean temperatures of the inflow component. The annual-mean total volume transports into the TIS, eTIS, wMUIS,
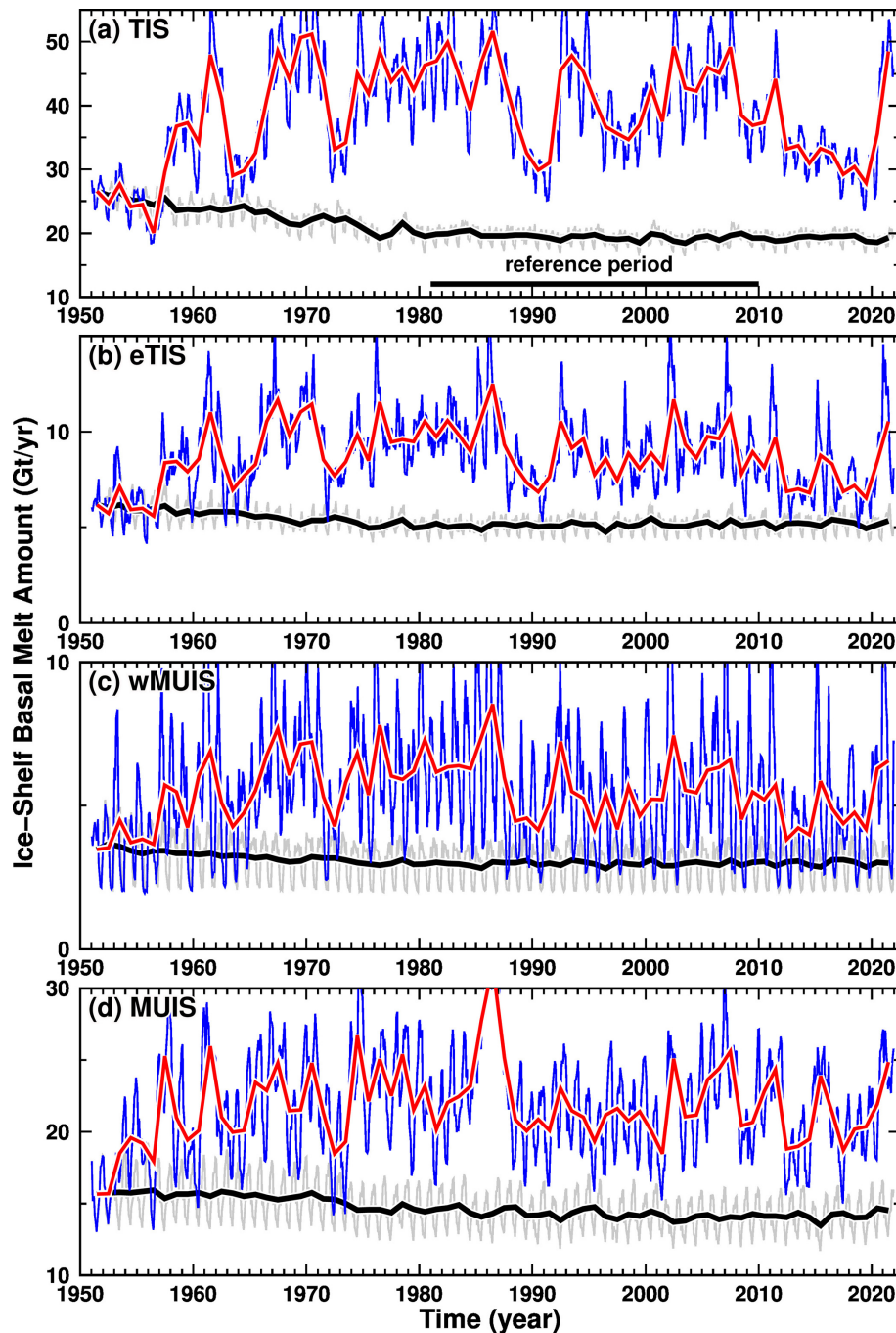
Figure 5. Time series of ice shelf basal melt amounts at four ice shelves along the Sabrina Coast, (**a** TIS, **b** eTIS, **c** wMUIS, and **d** MUIS), for the period 1951–2021. Blue and red lines show monthly and annual basal melt amounts, respectively; gray and black lines show results from the CKDRF case, which was forced repeatedly with the 1951 surface conditions to assess the model's inherent drift.

and MUIS are estimated to be 190, 48, 104, and 108 mSv, respectively. In the figure, the potential density boundary of 27.6 kg m^{-3} is shown as the green line for ease of comparison with the other figures. The annual-mean transport of water masses denser than 27.6 kg m^{-3} is represented by a dashed line to highlight the seasonality. There is a sizable inflow

of warm waters with temperatures higher than $-1.0\,°C$ in the densest layers (e.g., near the seafloor; see also Fig. 6), with the seasonal peaks occurring from May to September in the TIS and eTIS. The wMUIS reaches its peak in April–May and November–January, while the MUIS reaches its peak between October and January. Ocean heat transports
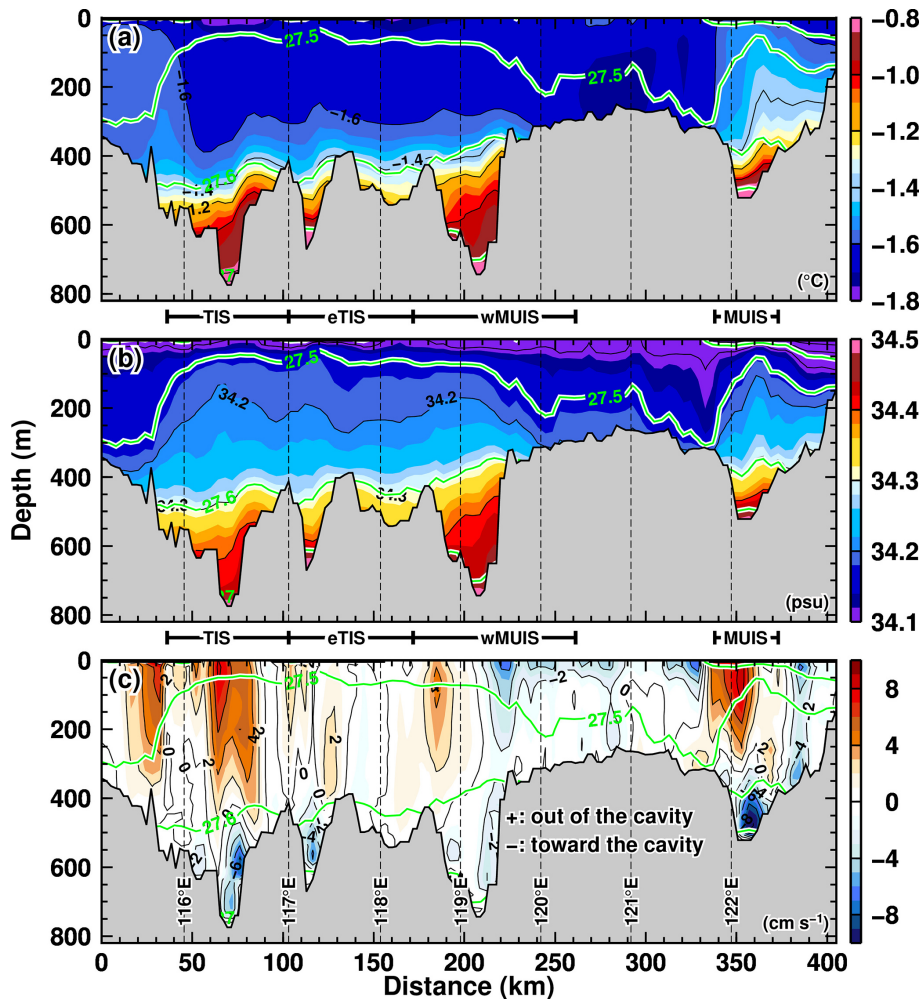
Figure 6. Vertical profiles of **(a)** potential temperature, **(b)** salinity, and **(c)** velocity along a line section located 5 km off the Sabrina Coast. The annual-mean variables averaged over the reference period (1981–2019) are used for the plots. Green contours indicate the potential density anomaly ($\mathrm{kg\,m^{-3}}$). Positive (negative) velocity indicates the ocean flow directed offshore (coast or ice shelf).

into the cavities show a similar seasonality (Fig. 7e–h). The annual-mean heat transports into the TIS, eTIS, wMUIS, and MUIS are estimated to be 723, 126, 331, and 331 GW, respectively. According to these analyses, the deep trough in front of the TIS cavity (Figs. 1b and 6) serves as an effective heat conduit from the Sabrina Depression to the TIS cavity. The wMUIS's volume and heat transports show characteristic seasonal changes. From June to October, there are signals of cold water inflow in the relatively less dense water masses, reflecting the cold water formation in the nearby coastal polynya during cold months. The existence of the seasonal cold water controls local heat transport into the cavity. A similar signal of seasonally formed cold water is observed at the TIS inflow during September and November, but its magnitude is small. Because the MUIS's front is covered with landfast ice, there is no such seasonal variation, and the volume and heat transports by deep warm water become large during October–December. The volume and heat

transport analyses demonstrate that the timing of deep warm water inflow differs from one ice shelf cavity to another.

We can extend the volume transport analysis described above to a vertical stream function by defining a semi-closed domain, which allows us to depict the ocean thermohaline circulation beneath an ice shelf (Fig. 8). It should be noted that this is the first modeling study to present the overturning circulation within the ice shelf cavities with realistic bathymetry and ice shelf draft (Hirano et al., 2023). We defined analysis sections in a semi-closed domain every 5 km from the ice front and performed the volume transport analysis (integrating the net volume transport laterally and from the dense to light water masses). Because solid lateral boundaries are required to form the semi-closed domain, the TIS and eTIS are combined for this analysis. The mean potential temperature averaged over the model grids between the sections is also shown in the figure. The three regions (TIS + eTIS, wMUIS, and MUIS) have clear overturning cir-
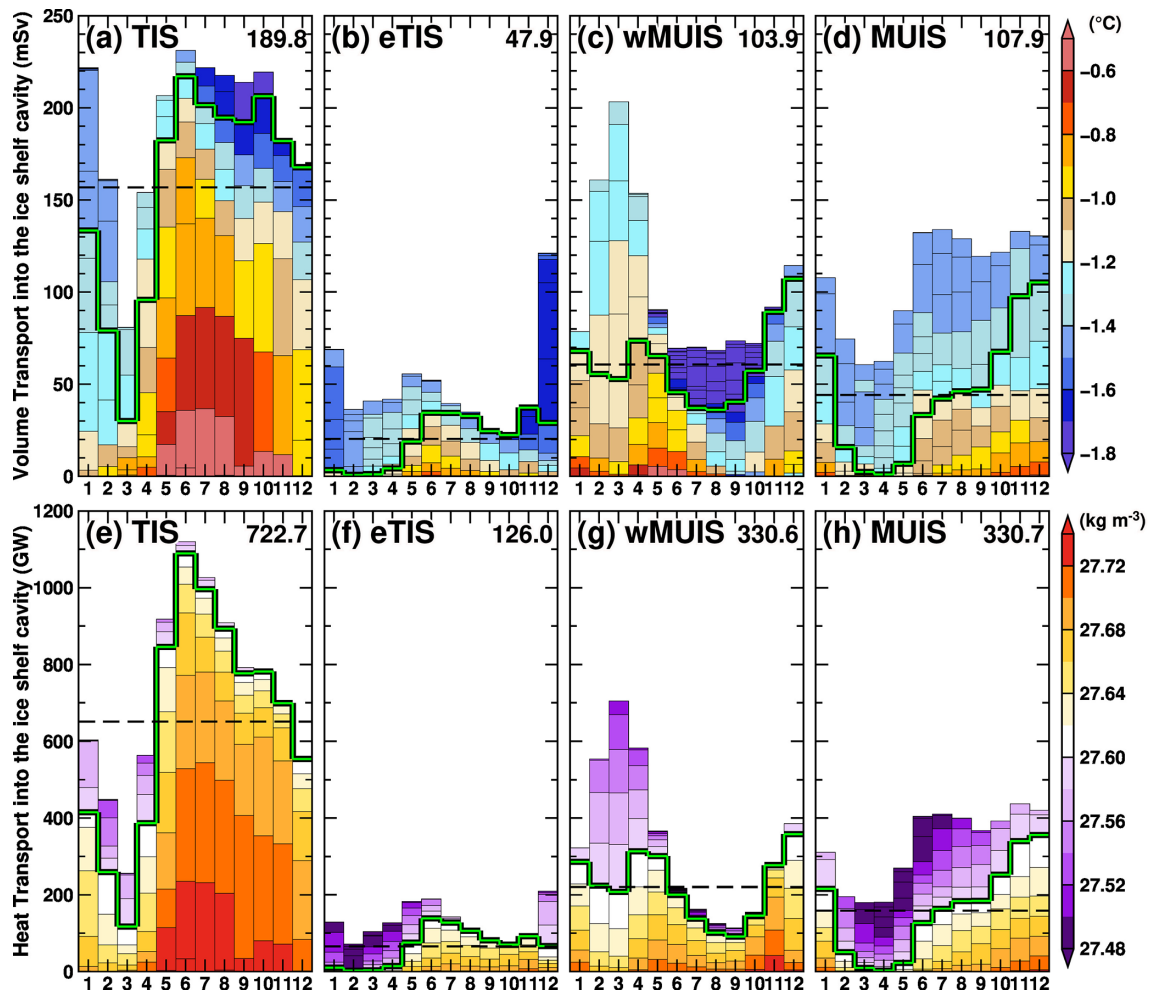
Figure 7. Seasonal variations in the net volume and heat transports into the four ice shelf cavities across the ice shelf front (TIS, eTIS, wMUIS, and MUIS from left to right). Colors in the upper **(a–d)** and lower **(e–h)** panels indicate potential temperature and density in $0.02\,\mathrm{kg\,m^{-3}}$ potential density bins. The green line shows the density interface of $27.60\,\mathrm{kg\,m^{-3}}$. The number on the right side of each panel indicates the annual-mean value. The dashed line in each panel shows the annual mean volume and heat transport of water masses denser than $27.60\,\mathrm{kg\,m^{-3}}$. All the variables are averaged over the reference period (1981–2010).

culations with deep warm water inflow and less dense cold outflow. The TIS + eTIS overturning circulation has about 200 mSv inflow across the ice shelf front, with a maximum value of over 240 mSv at a distance of 25 km poleward from the ice front. The density of the inflow ranges from 27.54 to $27.78\,\mathrm{kg\,m^{-3}}$ at the ice shelf front, but the bottom density of the inflow gradually decreases toward the inside, reaching $27.62\,\mathrm{kg\,m^{-3}}$ near the grounding line. The overturning circulation under the wMUIS is relatively short in length, and the opposite circulation forms in front of the ice shelf, partially reflecting cold, relatively dense water formation during cold months. The MUIS has a similar overturning circulation to the TIS–eTIS but with a much smaller magnitude.

5.2 Sabrina Depression

The analysis in the previous subsection indicates that warm deepwater inflow into the ice shelf cavities predominantly regulates the seasonal variation in the regional ice shelf basal melting (Figs. 4, 7, and S4). In this subsection, we take a closer look at seasonal variations in water mass exchange over the continental shelf to elucidate the water masses' linkage between the continental shelf region and ice shelf cavities. Here, we examine seasonal variations in water mass transport and the ocean temperatures across the western, northern, and eastern boundaries of the SD box placed on the continental shelf (the inset in Fig. 9). The control volume, the SD box, is the same one used in the sea ice production analysis (Fig. 3). The largest inflow transport into the SD box occurs across the eastern boundary, with an annual av-
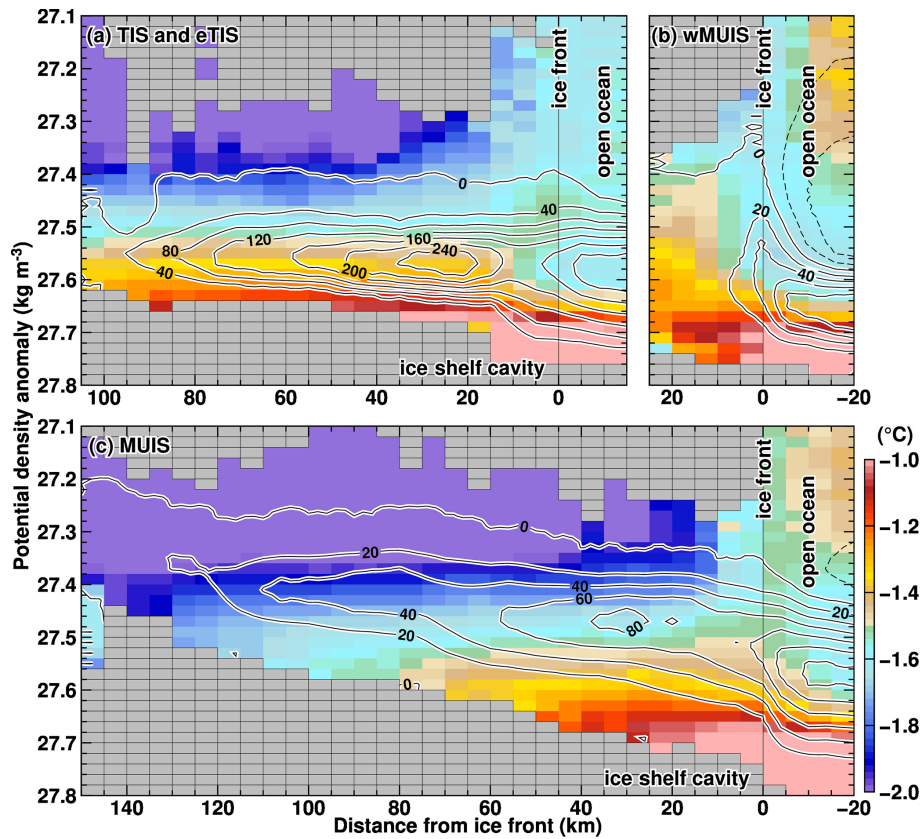
Figure 8. Vertical overturning circulations under **(a)** the TIS–eTIS, **(b)** wMUIS, and **(c)** MUIS cavities. Contours and colors show the overturning stream function (mSv) and ocean temperature in the distance–density space. The stream function is determined through the lateral integration of volume transport along consistent distances from the ice shelf within equivalent density layers. This integration process accumulates values from denser to lighter water masses. The horizontal axis is the distance from the ice shelf fronts, and the vertical axis is the potential density anomaly. The results show the annual-mean climatology averaged over the reference period (1981–2010).

erage transport of 590 mSv (Fig. 9c); it peaks from March to May, reaching approximately 800–1000 mSv. The outflow transport from the eastern boundary is minor throughout the year, with an annual average of about 40 mSv. The largest outflow transport from the SD box is across the western boundary, with an annual average of 642 mSv (Fig. 9d). The seasonal variation in the outflow transport is similar to the inflow across the eastern boundary, with the maximum from March to May approximately ranging from 800 to 950 mSv. Across the western and eastern boundaries, the inflowing and outflowing water masses have relatively light density classes (< 27.6 kg m^{-3}), and the water temperatures are relatively cold (< -1.6 °C). Looking at the inflowing water masses from the northern boundary, although the annual-mean inflow transport is moderate (282 mSv), warmer water inflows (> -0.8 °C) are identified in the dense water masses (> 27.6 kg m^{-3}). In the denser classes, the warmest water inflow occurs from October to January, and the water temperature is above 0 °C (Fig. 9b). The annual-mean outflow transport from the northern boundary is 207 mSv, with the peak during March–May and cold temperatures. This result

clearly shows that warm deepwater masses reaching the ice shelf originate from water across the northern boundary of the SD box (i.e., the shelf break).

To examine in detail the spatial pattern and seasonal progression of warm deepwater inflow onto the continental shelf across the shelf break, we present the annual-mean temperature averaged over depths deeper than 400 m (Fig. 10a) and a map of the month when the ocean temperature in each grid cell reaches its maximum (Fig. 10b). Furthermore, in Fig. 11, we use vertical profiles to illustrate the seasonal progression of the potential temperature and the potential density anomaly at four selected locations (shelf break, the Dalton Polynya, and two coastal regions in front of the ice shelves, labeled with A–D in Fig. 10). Warm deep water crosses the shelf break at 117–120° E and flows southeastward along the northeastern flank of the Sabrina Depression (e.g., a 600 m depth contour), forming a clockwise circulation. The warm deepwater intrusion fills the entire Sabrina Depression with water warmer than -0.6 °C. Near the coastal regions, although the ocean temperatures are colder than those in the central part of the depression, they are still above -1.0 °C,
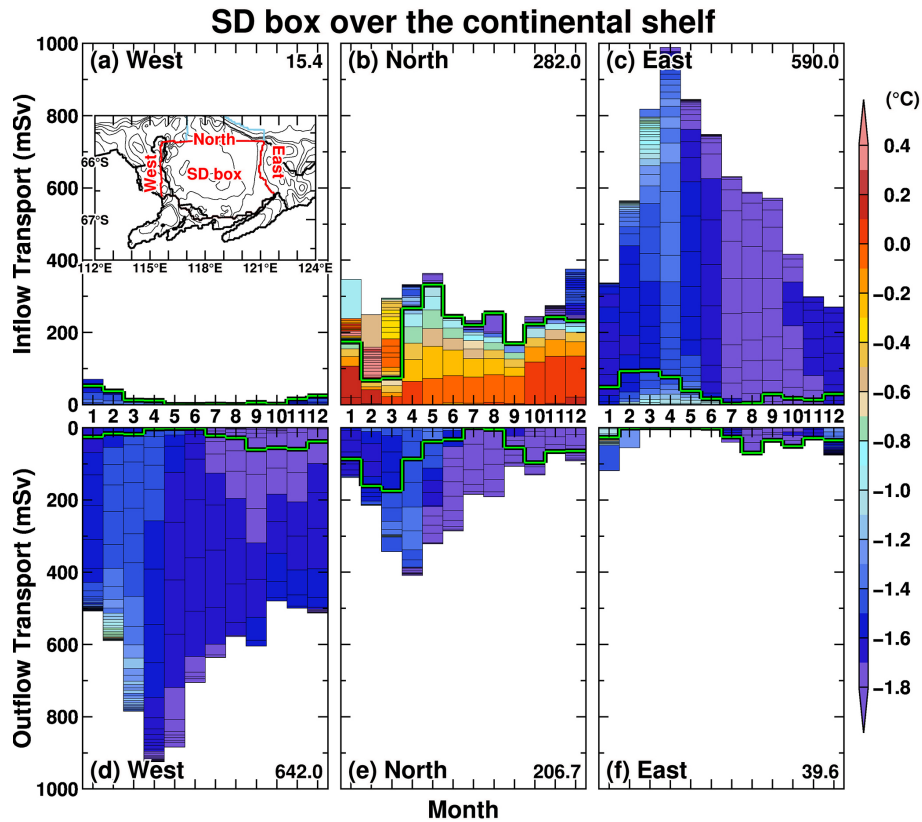
Figure 9. Seasonal variations in inflow and outflow volume transports across the boundaries of the SD box ((**a, d**) western boundary, (**b, e**) northern boundary, and (**c, f**) eastern boundary). Colors in the panels indicate the potential temperature in $0.02\,\mathrm{kg\,m^{-3}}$ density bins. The green line shows the density interface of $27.60\,\mathrm{kg\,m^{-3}}$. All the variables are averaged over the reference period (1981–2010). The number on the right side of each panel indicates the annual-mean volume transport. The inset in panel (**a**) shows the SD box (red) and slope box (light blue).

and the warm signals extend toward the ice shelves along the deep troughs (see also Fig. 6 for the vertical profiles). Along the shelf break and upper continental slope regions, the ocean temperatures peak during December–January, while over the continental shelf, the ocean temperatures are at their maxima from January to June, showing that the seasonal progression of the ocean temperatures differs greatly from one region to another.

In the shelf break region (Fig. 11a), the potential density surface of $27.7\,\mathrm{kg\,m^{-3}}$ is present at around 300 m throughout the year with only a small vertical variation, and there are warmer waters in the deep layers, with a potential temperature range from -0.6 to above $0\,°\mathrm{C}$. The ocean temperatures in the deep layers reach a maximum during November–February and a minimum during May–June. This seasonal progression at the shelf break explains the seasonal variation in the ocean temperature of inflow transport in the dense water classes to the SD box across the northern boundary (Fig. 9). In the Dalton Polynya (Fig. 11b), a cold surface mixed layer develops during the fall and winter seasons, when sea ice production becomes active (Fig. 3). For example, the $-1.6\,°\mathrm{C}$ isotherm gradually deepens after April,

reaching nearly 300 m depth by August. Below the seasonally developed mixed layer, there is a year-round signal of the warm water intrusion along the seafloor. The months of maximum and minimum ocean temperatures are December–February and August, respectively, and the seasonal progression is 1 to 2 months later than at the shelf break.

In front of the wMUIS (Fig. 11d), the seasonal progression is further delayed, with a maximum in May and a minimum in September–October. Here, the bottom ocean temperature in the maximum month is approximately $-0.7\,°\mathrm{C}$, and it is colder than that in the Dalton Polynya (Fig. 11b), reflecting successive water mass modification by interaction with the above cold mixed layer along the pathway of the clockwise ocean circulation. In front of the TIS (Fig. 11c), the ocean temperature reaches a maximum in June–August and a minimum in February–March. These results indicate that there is a profound time lag of about half a year between the shelf break and coastal regions, reflecting the slow clockwise ocean circulation in the Sabrina Depression. The lag is roughly accounted for by the timescale of the ocean circulation with typical current speeds of a few centimeters per second over the continental shelf. In both the coastal re-
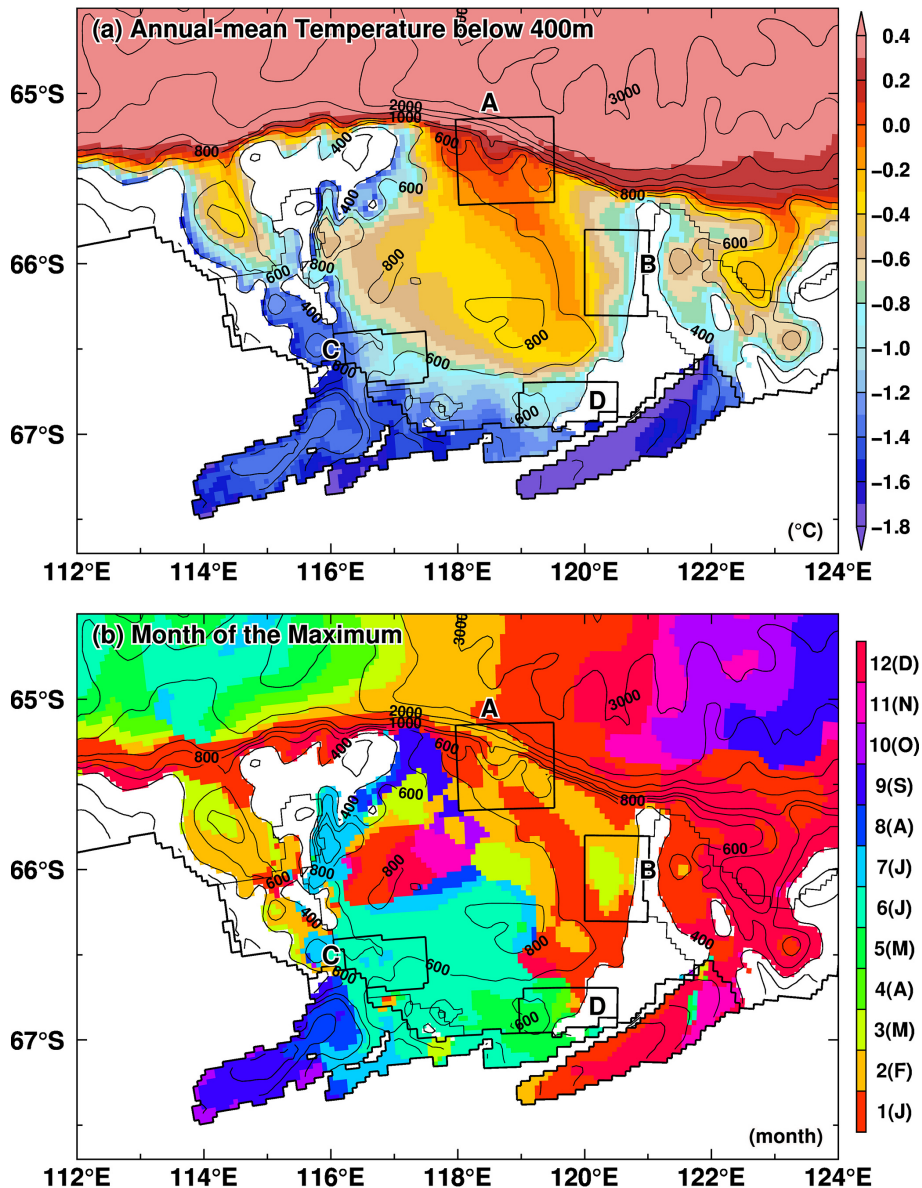
Figure 10. Horizontal distributions of **(a)** annual-mean ocean temperature averaged over depths below 400 m and **(b)** the peak month. These maps are based on the annual or monthly climatology for the reference period 1981–2010. Boxes labeled with A, B, C, and D show areas used for the vertical profiles in Fig. 11.

gions, although the thickness of the surface mixed layers in cold seasons is greater by about 100 m than that in the Dalton Polynya, there are warm water signals with the potential to become heat sources for intensive ice shelf melting.

5.3 Shelf break and upper slope regions

The analysis of inflow and outflow transport across the SD box's boundaries in Sect. 5.2 (Fig. 9) reveals that the intrusion of warm deep water onto the continental shelf predominantly comes from the northern boundary. In this subsection, in order to investigate water mass exchange between the open

ocean and the continental shelf regions, we place another control box over the shelf break and the upper continental slope regions (hereafter "slope box") and examine the inflow and outflow of water mass transport across the lateral boundaries (Fig. 12). The western, eastern, and northern boundaries of the slope box were set to 117° E, 121° E, and the 2500 m depth contour, respectively. The slope box's southern boundary shares a large part of the SD box's northern boundary, and thus the inflow and outflow across the slope box's southern boundary correspond to the outflow and inflow, respectively, across the SD box's northern boundary (Fig. 9e and b). We only calculated the inflow and outflow
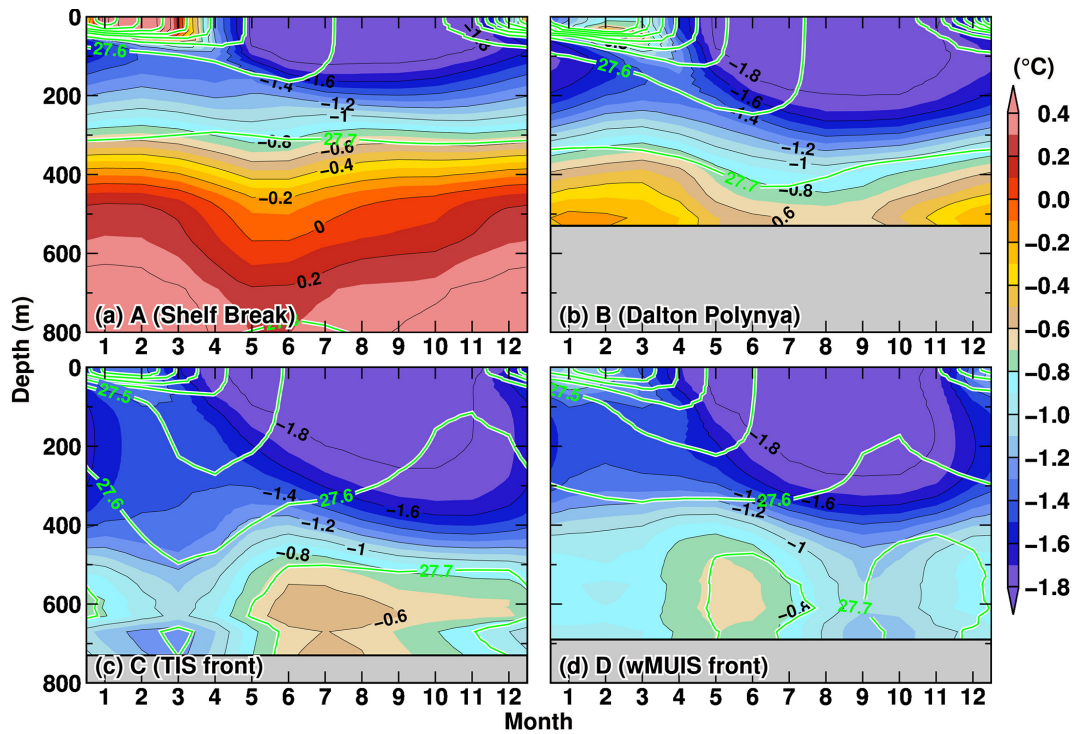
Figure 11. Seasonal variation in potential temperature (background colors) and potential density anomaly (green contours; kg m^{-3}) averaged over the boxes in Fig. 9. The panels are based on the monthly climatology for the period 1981–2010.

transports from the surface to 800 m to focus on water mass exchange across the shelf break, which has a depth of less than 650 m. On an annual-mean basis, there is a substantial inflow from the eastern boundary into the slope box, with the total transport over 1000 mSv (Fig. 12c). Balancing this annual-mean inflow transport, there are outflow transports exceeding 400 mSv at both the western and northern boundaries (Fig. 12d and e), southward transport to the SD box (Fig. 9b and e), and downward transport across the 800 m interface. As shown later (Figs. 13 and 14), offshore water flowing across the shelf break to the continental shelf region resides on the upper continental shelf. Therefore, in this section, we focus on the lateral inflow and outflow patterns. The lateral inflow or outflow pattern becomes more prominent from March to September, reflecting the facts that the stronger easterly wind drives the westward-flowing ASC (Fig. 2) and the ASC flows through the box. Interestingly, the inflow or outflow pattern from November to January differs markedly. Warm water inflows in the dense water classes come from the western and northern boundaries into the box and outflows from the eastern boundary, indicating the existence of seasonal eastward-flowing currents in the subsurface layers (e.g., undercurrent). Focusing on dense water masses (> 27.6 kg m^{-3}) in these months, there are inflow transports ranging from 100 to 200 mSv, with the ocean temperature reaching +0.4 °C. As shown below, in the summer months, an eastward-flowing undercurrent forms beneath the

ASF/ASC, controlling the warm deepwater intrusions across the shelf break into the continental shelf region.

Figures 13 and 14 show the velocity fields in December, June, and September in the surface (0–100 m) and middle-depth (400–600 m) layers, respectively. The westward-flowing ASC develops in the surface layer in June and September (Fig. 13b and c), and the signals are identified in the middle-depth layer (Fig. 14b and c). In December, the flow pattern along the shelf break is substantially different. There is relatively modest westward surface flow, and a broadly structured eastward-flowing undercurrent forms in the region between the 500 and 2000 m depth contours (Fig. 14a). Figure 15 shows the vertical profiles of east–west ocean velocity and temperature in December and September along the 117° E line. The vertical profile of the ocean velocity clearly delineates the outline of the eastward-flowing undercurrent, which forms in the 200 to 1000 m depth range and meridionally from 65.2 to 65° S, just north of the surface core of the ASC. The undercurrent has a maximum velocity of approximately 5 cm s^{-1}, and the core is located near a depth of 500 m. The depth of the undercurrent core is shallower than that of the central trough of the Sabrina Depression (see the blue line in Fig. 15). In September, when the ASF is most developed, the westward flow extends from the surface to the seafloor over the shelf break and upper continental slope regions. The seasonal transports of the surface current and undercurrent are shown in Fig. S6 in the Supplement.
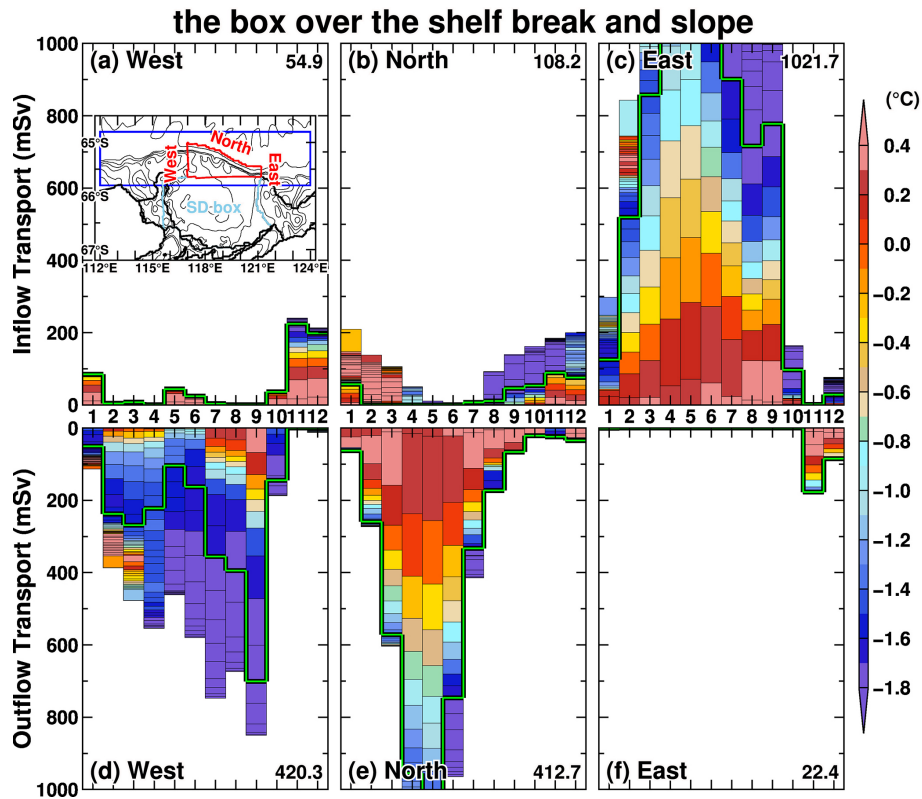
Figure 12. As in Fig. 9 but for the slope box. The blue box in the inset shows an area for Figs. 13 and 14, and the red and light-blue lines show the slope and SD boxes, respectively.

We calculated the transports of the surface current by integrating the westward transport in density layers lighter than $27.7\,\mathrm{kg\,m^{-3}}$ and that of the undercurrent by integrating the eastward transport in density layers denser than $27.6\,\mathrm{kg\,m^{-3}}$. We treat the density layer in 27.6–$27.7\,\mathrm{kg\,m^{-3}}$ as a transition layer between the ASF and the seasonally formed undercurrent (Fig. 15). The surface current transport becomes small from November to January and reaches its maximum in September. The undercurrent transport reaches its minimum in September, starts to increase from October, and reaches its maximum in November–December. It should be noted that, although the eastward transport increases from April to July, this is not due to the structure of the undercurrent in the west–east direction but is instead due to the small-scale local circulation of the flows in from the western boundary and out to the northern boundary (Fig. 14b).

6 Causes of interannual variability in the regional ocean–cryosphere interactions

As seen in Figs. 5 and S5, there is considerable low-frequency interannual variability (timescales longer than 5–7 years) in the ice shelf basal melting along the Sabrina Coast. In this section, we examine relationships among the ocean–cryosphere variables in terms of interannual variabil-

ity. Figure 16 presents the correlation coefficients between the variables of the sea ice production over the Sabrina Depression ("SP" in the figure), the ocean heat transports across key sections ("HT"), the ocean overturning circulation beneath the ice shelves ("OVT"), and the ice shelf basal melting ("BM"). Annual averages were used in this analysis. The lower-left half of the plot shows the correlation coefficients between a pair of variables after taking a 7-year running mean to focus on low-frequency interannual-to-decadal variations, and the upper-right half shows them after removing the running mean from the original annual-mean time series to focus on high-frequency year-to-year variations. The heat transports are the southward component across the northern boundary of the SD box ("nSD") and the inflow components across the ice fronts (short abbreviations of wM, eT, and TI representing wMUIS, eTIS, and TIS, respectively, in Fig. 16).

There are robust positive correlations between ice shelf basal melting at the TIS and the neighboring ice shelves, especially in the low-frequency variability (eTIS: $r = 0.96$; wMUIS: $r = 0.90$). The correlation with the eTIS remains high for the high-frequency variability ($r = 0.86$), but it decreases to $r = 0.71$ for the more distant wMUIS, indicating that a different factor contributes to the high-frequency year-to-year variability in ice shelf basal melting at the wMUIS.
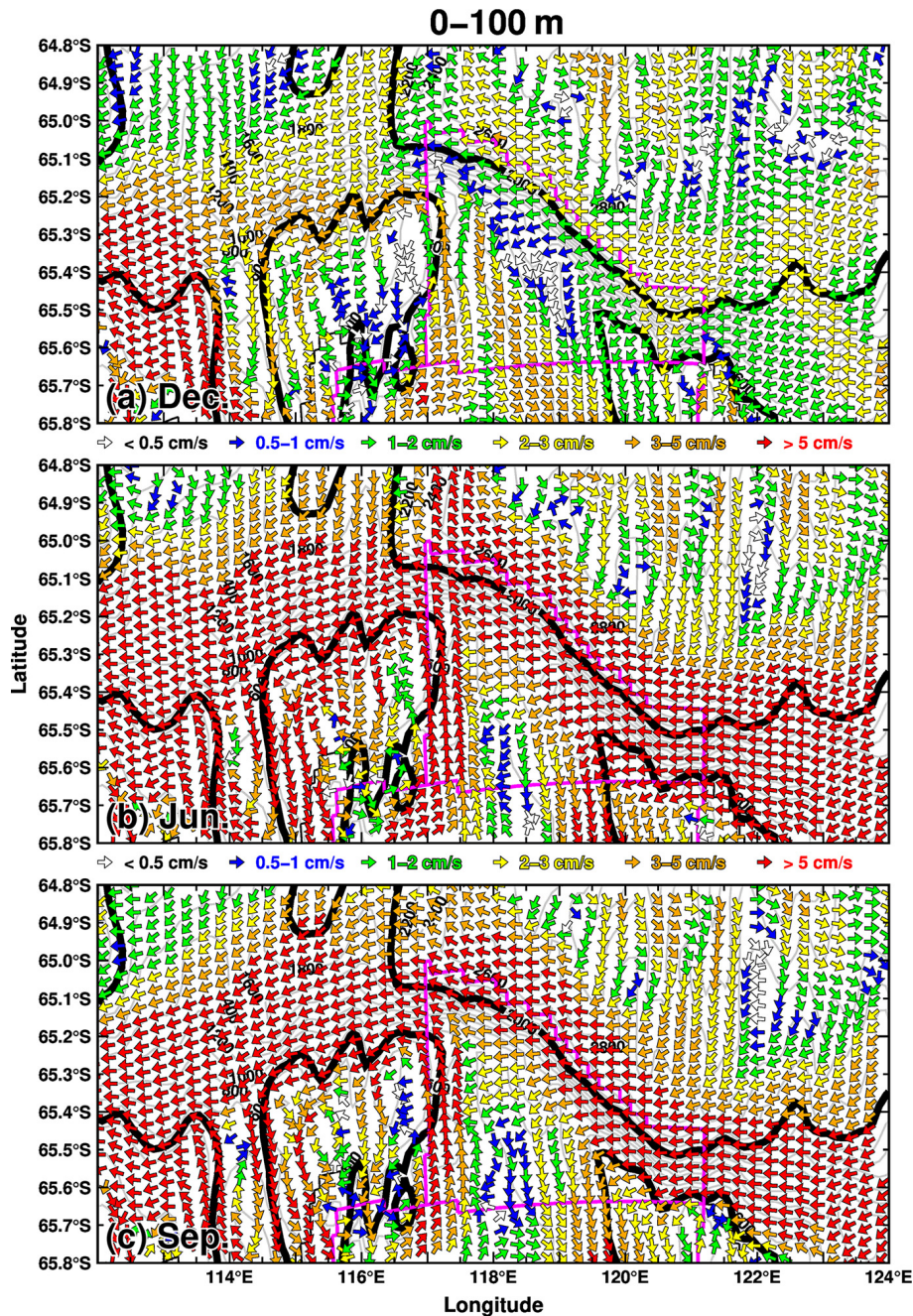
Figure 13. Maps of ocean flows in the depth range from the surface to 100 m in **(a)** December, **(b)** June, and **(c)** September. The vector shows the ocean flow direction, with color showing the magnitude. The thick black curves show the 500 and 2000 m depth contours, and the gray curves show the depth contour with 200 m intervals. The magenta line indicates the boundaries of the slope and SD boxes.

The most notable feature of this figure is that the southward ocean heat transport across the SD's northern boundary has positive correlations with ocean heat transports towards ice shelf cavities, the overturning circulation within the cavities, and the ice shelf basal melting. This indicates that the fluctuation of warm deepwater intrusions into the Sabrina Depression is a common driving force of the interannual variability in these components. In particular, they far exceed the 95 %

significance level in the low-frequency variability. Sea ice production is negatively correlated with most of these components. In particular, in the high-frequency variability, there is a significant negative correlation between ice shelf basal melting and sea ice production, indicating that the cold water formation associated with sea ice production erodes some of the warm deepwater inflow into the ice shelf cavities. In summary, the fluctuation in warm deepwater intrusions across the
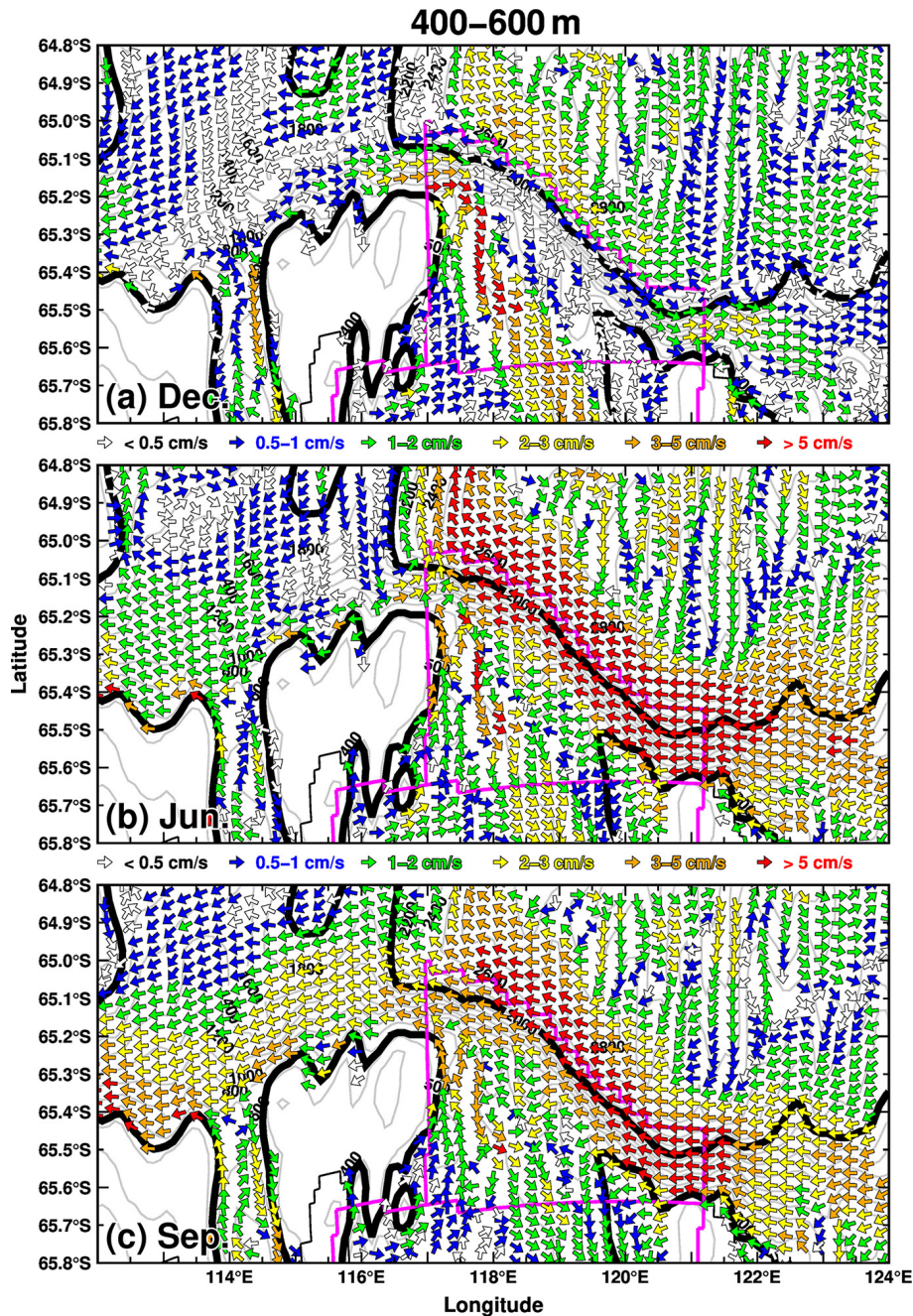
Figure 14. As in Fig. 13 but for a depth range from 400 to 600 m.

shelf break determines the low-frequency variability in ice–ocean interactions along the Sabrina Coast, whereas the high-frequency year-to-year variability is determined by a combination of the local sea ice production and the warm deepwater intrusions.

Seasonal variations in the southward ocean heat transport across the SD's northern boundary reveal that the intrusion of warm deepwater intrusion into the continental shelf regions occurs throughout the year (Fig. 9b), with the warmest water entering in summer. The analysis of inflow and outflow transports across the slope box's boundaries, which fuel the southward heat transport, revealed that the inflow pattern of warm deep water varied significantly depending on the season, with the warm deepwater inflow in summer transported by the eastward-flowing undercurrent and that in the other seasons carried by westward flow in the well-developed ASF/ASC system. Therefore, here we use the two periods of November–January and March–September to investigate
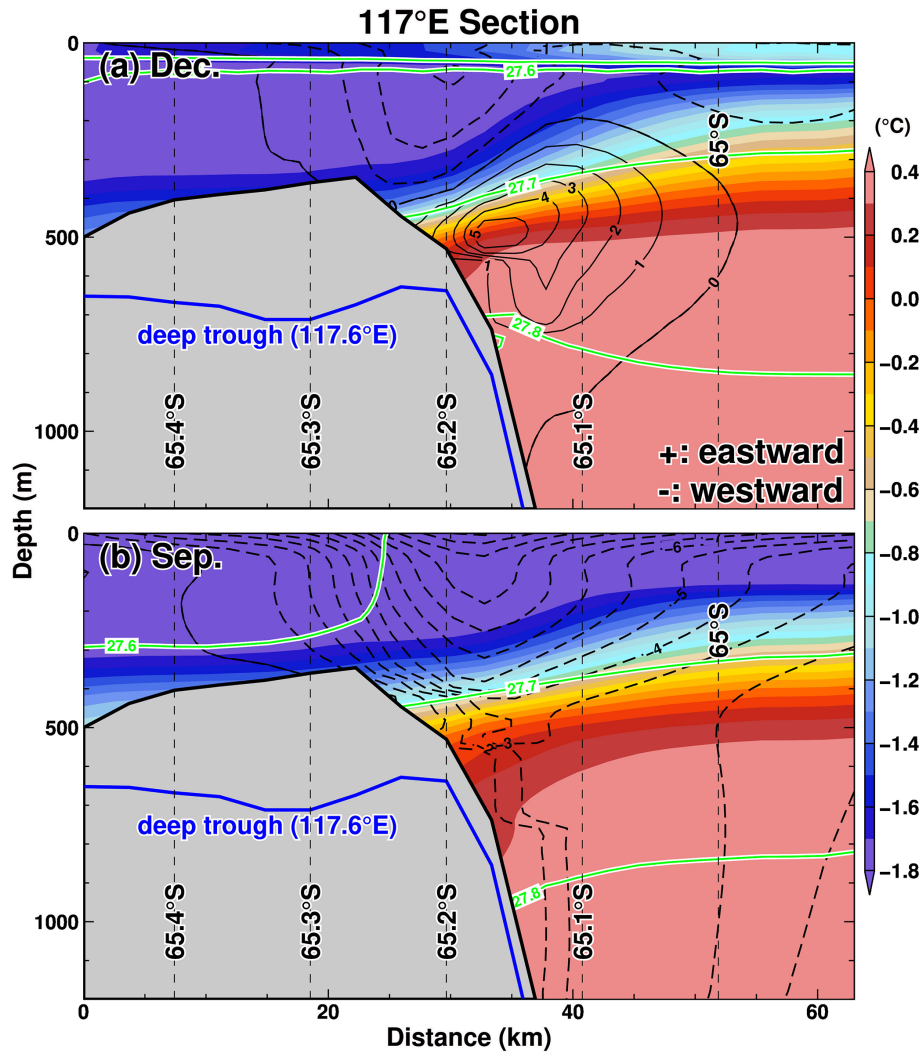
Figure 15. Vertical profiles of potential temperature (background colors), potential density anomaly (green contours), and east–west velocity (black contours) along 117° E in **(a)** December and **(b)** September. The blue line shows the bottom topography along the 117.6° E section. Positive and negative values of the velocity indicate eastward and westward, respectively. The variables averaged over the reference period 1981–2010 are used for the plots.

the interannual variability in the ocean currents over the upper continental slope causing warm deepwater intrusions and their relationship with coastal wind (Fig. 2), which would be the driving force of the ocean currents. The months of February and October were assumed to be transition months and were excluded from this analysis.

The southward heat transport time series (Fig. 17a) explain the TIS basal melting (Fig. 5), as seen in the very high correlations between the two (Fig. 16). We found that the ocean heat transport from the western boundary to the slope box is negatively correlated with wind speed ($r = -0.41$, over the 95 % significance level) from November to January. This means that when the summertime wind speed is low, an eastward-flowing undercurrent develops. In contrast, from March to September, when wind speeds are strong, the

ASF develops from the surface to deep layers, and the overall westward-flowing current delivers the ocean heat from the eastern boundary to the slope box. In summary, the origins of ocean heat transport to the Sabrina Depression vary greatly depending on the season; interestingly, the responses of the eastward-flowing undercurrent and westward-flowing ASC in ASF to wind speed are totally opposite. The magnitude of the correlation coefficient between the southward ocean heat transport across the SD's northern boundary and wind speed ($r = -0.32$) is smaller than those for the two periods of the year ($r = -0.41$ and $r = +0.44$), reflecting the opposite responses of the two ocean currents to the wind variability. The correlation coefficient of the southward heat transport with the eastward heat transport by the undercurrent, $r = +0.23$, is higher than that with westward heat transport
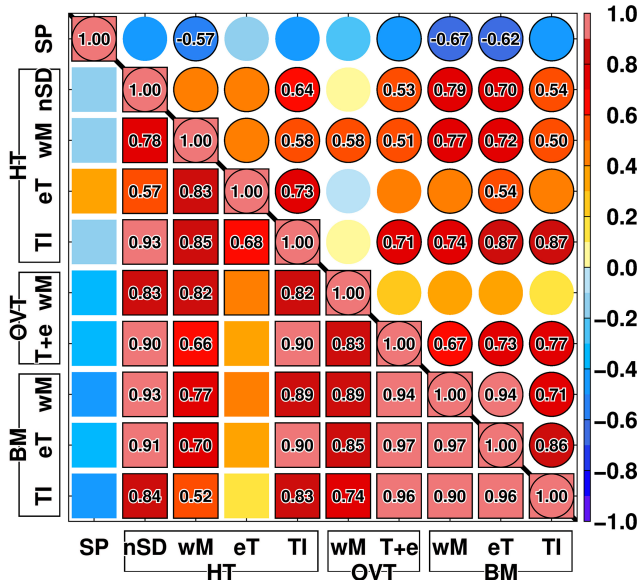
Figure 16. Correlation coefficients between two variables. The variables are sea ice production (SP), heat transport (HT), overturning circulation (OVT), and ice shelf basal melting (BM). The short abbreviations nSD, wM, eT, TI, and T + e stand for the northern boundary of the SD box, western MUIS, eastern TIS, TIS, and TIS + eTIS, respectively. Squares show correlation coefficients after 7-year running mean data, and circles show correlation coefficients after removing the running mean. Marks enclosed with black lines indicate an exceeding 90 % confidence level (0.43), and numbers indicate an exceeding 95 % confidence level (0.50). The confidence levels are estimated from the Monte Carlo methods (generating random samples, taking a 7-year running mean, estimating the length of autocorrelation, and calculating effective degrees of freedom). The same confidence levels are used for the high-frequency year-to-year areas (circles).

Figure 17. Time series of ocean heat transport and wind speed. Colored lines in panels **(a)**, **(b)**, and **(c)** are the southward component across the SD box's northern boundary averaged over the year, the eastward components across the slope box's western boundary averaged from November to January, and the westward components across the slope box's eastern boundary averaged from March to September, respectively. The correlation with the coastal wind speed averaged over the yellow box in Fig. 2 is shown in the upper-right corner. In panel **(a)**, correlations of the annual-mean heat transport with the eastward and westward heat transports are shown in red and blue, respectively.

by the ASC ($r = -0.09$), indicating that the fluctuation in the summertime undercurrent mainly regulates the interannual variability in the heat transport onto the Sabrina Depression and the subsequent ice shelf basal melting. Finally, we calculated correlation coefficients with the Southern Annular Mode (SAM) index, an indicator of changes in atmospheric circulation over the Southern Ocean. The SAM index in this study was calculated from the difference in the normalized zonal mean sea level pressure at 65 and 40° S (Gong and Wang, 1999). Correlation coefficients between wind speed and the SAM index are -0.70 in November–January and -0.47 in March–September, which exceed the 95 % significance level ($r = 0.23$). This means that a positive value in the SAM index leads to weaker coastal winds (Neme et al., 2022). The correlation coefficients of the undercurrent and ASC with the SAM index were $+0.28$ and -0.42, respectively. As with the response to wind speed, the undercurrent and ASC responses to the SAM are totally opposed.
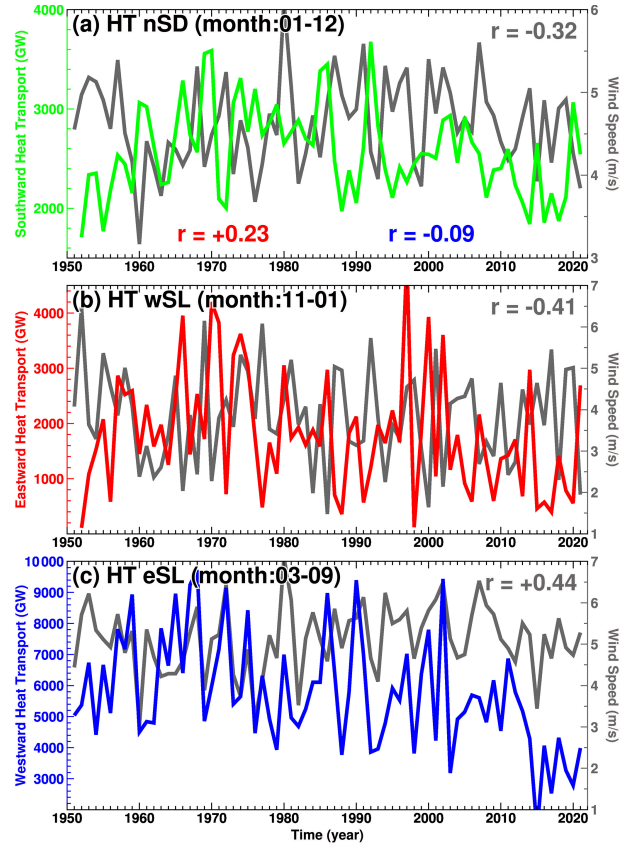
7   Summary and discussion

The study is the first to simulate and investigate comprehensive ocean–cryosphere interactions off the Sabrina Coast over 70 years (1951–2021), including the ocean heat transport from the shelf break and upper slope regions to the continental shelf, the regional ocean circulations and properties over the Sabrina Depression, the water mass exchanges across the ice shelf fronts, the overturning circulations within the cavities, and the overall ice shelf basal melting. Previous modeling studies have focused on specific aspects contributing to the ice–ocean interactions in this region. While valuable, there has been little discussion about the relative importance of each aspect from the overall perspective of the regional ocean–cryosphere interactions. The study is novel

through its use of updated bathymetry to configure an ocean–sea ice–ice shelf model (Figs. 1 and A1) for detailed analyses of seasonal variations in the sea ice fields, ocean fields, and ice shelf basal melting. Importantly, the model has a long-term integration spanning more than 70 years, making the output suitable for examining seasonal and interannual-to-decadal variability. While a direct comparison between our model's TIS basal melting (Fig. 5a) and observational data is challenging, we find our model's interannual variability to be consistent with the observed variability and trends, including the temperature rise over the continental shelf from 2015 to 2022 (Rintoul et al., 2016; Hirano et al., 2023), the decrease in ice discharge after 2010 within the 2008–2018 observation period (Miles et al., 2022), and the long-term TG acceleration since the 1960s (Li et al., 2023). The model is subject to constraints and uncertainties, including assumptions such as a stable ice shelf shape, sub-ice shelf topography, and ice–ocean parameterization. Additionally, uncertainties related to factors like the time lag in ice sheet or shelf response to ocean forcing through basal melting make direct comparisons across different variables more challenging. However, within these limitations, our findings do not contradict existing observations and provide new insights into interannual-to-decadal variability.

The Antarctic coastal region is subject to easterly winds throughout the year, with a maximum in winter and a minimum in summer (Fig. 2). This easterly wind is the driving force of the ASF/ASC system (Thompson et al., 2018). This model shows that the ASF is well developed from the surface to the middle levels, with the stronger ASC in winter when the easterly wind is stronger (Figs. 13b and c, 14b and c, 15b, and S6). Conversely, during the summer months from November to January, when the coastal easterly wind is weak, an eastward-flowing undercurrent is clearly present at depths of 400–800 m just beneath the westward-flowing ASC (Figs. 13a, 14a, 15a, and S6). The interannual variations in both current systems are significantly correlated with easterly wind speed, but their signs are opposite (Fig. 17). The model reproduces the year-round intrusion of warm deep water into the continental shelf (Fig. 9b). Since the depth of the shelf break to the north of the Sabrina Depression is 500–600 m, the wintertime ASC variation at middle depth and the summertime undercurrent are important for regulating the warm deepwater intrusion. The warmest water of the intrusion occurs during the summer season (Fig. 9), and it originates from the eastward-flowing undercurrent on the upper continental slope (Fig. 12). The warmest signals near the shelf break are slowly carried toward the coastal regions and the TIS by the clockwise ocean circulation formed over the Sabrina Depression (Figs. 10 and 11). The high sea ice production of the Dalton Polynya (Figs. 3 and S2) can substantially alter the water masses at the surface and medium depths, while the warm signals from the deepwater intrusion remain present along the seafloor (Figs. 6 and 11). The warm signals can also be detected in the seasonal variations in the coastal wa-

ter masses flowing into the TIS cavity (Fig. 7). The cold water masses associated with local sea ice formation are clearly visible in the wintertime inflow into the wMUIS cavity located south of the Dalton Polynya, whereas warm deep water dominates the inflow at the other ice shelf cavities throughout the year. This modeling framework is the first to illustrate ocean overturning or thermohaline circulation within the ice shelf cavities in a realistic configuration, with warm inflows in deep layers and outflows of lighter, colder water at shallow depths (Figs. 6 and 8). The seasonal variation in ice shelf melting varies with distance from the ice shelf front, and the TIS has its maximum from September to November near the grounding line (Figs. 4 and S4). The interannual variability in the TIS basal melting has a predominant periodic variability of about 5–11 years (Figs. 5 and S5). The mCDW intrusion into the continental shelf region is the root cause of this low-frequency variability (Fig. 16). The mMUIS exhibits a similar low-frequency variability, although the seasonal fluctuation caused by convection associated with the sea ice formation dominates the local variability (Fig. S5).

Despite these promising results, it is important to point out several limitations of this study and the differences from the previous studies. Using the updated bathymetry, we constrained the regional bathymetry of the Sabrina Depression, particularly the coastal regions in front of the ice shelves, which are crucial for representing inflows of warm deep water to the cavities. However, as shown in Fig. A1, there are still large uncertainties in the bathymetry over the entire continental shelf. Since the representation of bathymetry in a high-resolution ocean model is directly linked to the reliability of the modeled ocean currents and properties, it is hoped that these regions of uncertain data will be quickly resolved by future surveys. The present model has a horizontal resolution of 3–4 km for the target area (Fig. 1), and we were able to reproduce the bathymetry-guided ocean flow patterns from the shelf break to the continental shelf and ice shelf regions. It should be noted that the raw bathymetry data have smaller structures within the deep troughs ranging from several hundred meters to 1 km, and such small-scale bathymetric features that cannot be resolved in this model may have a significant impact on the modeled ocean flow patterns. There is also a limitation regarding the bathymetry under the ice shelf in this model, and very recent research by Vaňková et al. (2023) underscored the influence of under-ice-shelf bathymetry on ice shelf basal melting. For instance, the accuracy of the bathymetric data underneath ice shelves can greatly affect the representation of circulation under the ice shelf. The ocean velocity at the ice shelf bases has an impact on both the patterns and magnitudes of ice shelf basal melting. This effect is especially pronounced when a velocity-dependent parameterization is used for thermal and salinity exchanges at the ice–ocean interface (Mueller et al., 2012; Dansereau et al., 2014). It is worth noting, however, that this study employed a velocity-independent parameterization. While this approach captures the ice shelf basal melting driven primar-

ily by the dominant thermal forcing originating from the mCDW intrusion, it cannot account for secondary effects like enhanced melting patterns due to buoyancy-driven upslope flows generated by the upstream ice shelf meltwater. In scenarios where velocity-dependent parameterization is used, the melting pattern in the model might change in regions with stronger currents, offering a potentially more intricate view of the ice–ocean interactions. Incorporating the updated datasets, e.g., the inversion bathymetry from Vaňková et al. (2023) for grounding line zones, into numerical models at each stage could further refine our understanding of ocean–ice interactions, potentially revealing more nuanced basal melt patterns and circulations beneath the ice shelves. This is a promising direction for future research, which will contribute to a more detailed and accurate understanding of these complex ocean–cryosphere interactions.

While the results of this study are consistent with previous works linking the magnitude of mCDW intrusions to the strength of the wind-driven ASF/ASC in the surface layer, this study elucidates a different mechanism. Previous studies have proposed that the thickness and transport of the mCDW are determined in response to the vertical fluctuation of the lower-density surface of the ASF; e.g., the weaker the ASF, the more the mCDW intrusion (Nakayama et al., 2021). The present model results show that the density variability near the shelf break regions is limited to shallow depths (< 200 m) and that temperature changes in the deep layers are not linked to the vertical density fluctuation (see the potential density of 27.7 kg m^{-3} in Fig. 11a). Instead, we find that seasonal variations in the eastward and westward flows at middle depths over the upper continental shelf (Fig. 12) are responsible for the mCDW intrusion into the Sabrina Depression (Fig. 9). This discrepancy between the models may be related to whether or not the eastward-flowing undercurrent is reproduced. We consider that the present model result is feasible for the following reasons. From the observational perspective, eastward-flowing undercurrents beneath the ASF are often detected along the Antarctic coastal margins (Chavanne et al., 2010; Heywood et al., 1998; Núñez-Riboni and Fahrbach, 2009; Walker et al., 2013; Peña-Molino et al., 2016). According to Peña-Molino et al. (2016), mooring observations at 113° E revealed that the eastward-flowing undercurrent forms beneath the westward-flowing ASF in the East Antarctic coastal region. From a modeling perspective, several recent studies (Silvano et al., 2022, 2019; Kusahara et al., 2021; Assmann et al., 2013; Smedsrud et al., 2006) demonstrated that representing the undercurrent on the upper continental slope plays a crucial role in mCDW intrusion and ice shelf basal melting. Note that, while the undercurrent disappears seasonally in the East Antarctic region, it persists year-round in the West Antarctic region (Silvano et al., 2022).

Given that the origin of the warm deep water flowing into the Sabrina Depression varies seasonally and that the possible warm water sources are widely distributed east to west over the continental slope and rise, it is therefore essential to understand how the ocean conditions are set up over the entire large area off the Sabrina Coast. The Totten area is located in the eastern part of the Kerguelen Gyre in the Australian Antarctic Basin, where the Antarctic Circumpolar Current (ACC) deflects southward, bringing warmer offshore waters closer to the coastal regions. The interaction between the two strong currents (ACC and ASF/ASC) and the rugged seafloor topography forms steady cyclonic eddies over the continental rise, which play a role in the north–south ocean heat transport between the deep and coastal oceans (Wakatsuchi et al., 1994; Mizobata et al., 2020; Hirano et al., 2021). The combination of the ACC location and the cyclonic eddy chain is thought to have a widespread impact on the ocean conditions over the continental slope and rise regions.

Recent studies from hydrographic and satellite observations imply a long-term southward migration of the ACC fronts in the Australian Antarctic Basin, which may promote more warm water toward the coastal regions (Yamazaki et al., 2021; Herraiz-Borreguero and Naveira Garabato, 2022). Linear trends of the model's TIS basal melting and the ocean heat transport to the Sabrina Basin over the entire integration period are positive and do not contradict these observations (Fig. 5). However, to fully investigate this proposed mechanism of the interaction between the offshore conditions and ice shelf basal melting, numerical experiments with longer integration periods or experiments in which the ACC front locations in the model are artificially modified would be required. Furthermore, better knowledge of the role of the cyclonic eddies over the continental slope and rise regions, which directly connect deep ocean and continental slope regions, is also necessary. Here, we briefly conjecture the ocean responses by the major atmospheric mode, SAM. It is well known that the SAM index has a positive trend over the decades, and the trend is expected to continue under a global warming condition (Bracegirdle et al., 2013; Zheng et al., 2013). The positive SAM indicates stronger eastward wind components over the Southern Ocean, leading to stronger westerly wind over the ACC region and weaker coastal easterly wind (Neme et al., 2022). The plausible changes in wind fields may cause more southward ocean heat transport by the ACC and a stronger undercurrent in summer, causing more active ice–ocean interaction along the Sabrina Coast.

Although it has been recognized that the Antarctic slope undercurrent plays a key role in water mass exchanges between the deep and coastal oceans, its dynamics are not yet fully understood. Based on the results of this study, the bathymetry and seasonal variations in ocean stratification and alongshore wind are expected to be factors responsible for the formation. To investigate the dynamics of the slope undercurrent in more detail, numerical experiments in which these components are simplified or idealized would be helpful. Once the undercurrent dynamics are understood, it will be feasible to determine where and how the undercurrent changes will occur in an ongoing warming world. This will

lead to a better understanding of not only changes in the inflow of warm deep water onto the continental shelf, but also changes in the Antarctic ice shelf basal melting, inner ice sheet mass balance, and sea level rise.

Appendix A: Comparison of the compiled data with existing bathymetry datasets

Several numerical ocean modeling studies have been conducted on the Sabrina Coast, but they used different bathymetry datasets. In low-resolution ocean models (e.g., 1°) or regions where the water depth is well constrained, the differences between the datasets would not be much of an issue in creating a model bathymetry. In high-resolution ocean modeling with a resolution of several kilometers, it is vital to prepare reliable bathymetry in the focal region. Model bathymetry accuracy is directly linked to the reproduction of ocean circulation in the model. Particularly on the Antarctic coastal margins, poleward CDW intrusions from shelf breaks to continental shelves, which are strongly constrained by local bathymetry (Nitsche et al., 2017), play an important role in ocean–cryosphere interactions. In this study, we created a model bathymetry to combine the recently compiled bathymetry over the Sabrina Depression (Hirano et al., 2023) and BedMachine near or underneath the ice shelves. It should be noted that the ocean bathymetry in BedMachine is a blend of the International Bathymetric Chart of the Southern Ocean (IBSCO) (Arndt et al., 2013) for the background and additional sources of the regional refinements (Morlighem et al., 2020). For the Totten Ice Shelf, the inversion product from Greenbaum et al. (2015) was used.

Here, we compare several bathymetric datasets with direct measurements and justify the model's bathymetry, with a focus on the shelf break region and three regions over the continental shelf. The three selected regions are the eastern and central parts of the Sabrina Depression and a coastal region in front of the TIS, labeled with x, y, and z, respectively, in Fig. A1b. Firstly, the shelf break in the observation and all the datasets (e.g., the 1000 m depth contour) are identified within a latitude range between 65.5 and 65° S. The depth contours representing the shelf break in the observation, GEBCO2020, and ETOPO1 are found to smoothly extend in the east–west direction, whereas those in BedMachine and RTopo-2 have unrealistic or artificial bumps along the shelf break, which probably originated from gravity inversion processes. Secondly, the observed water depth in area x is shallower than 400 m, and it is thus an effective topographic barrier between the Sabrina Depression and east of 121° E. This bathymetric feature is captured in GEBCO2020 and RTopo-2, whereas in BedMachine and ETOPO1, there is a wide trough-like structure (> 500 m) that differs from the observed one. Thirdly, the central part of the depression is deeper than 800 m (see region y). GEBCO2020 and Bed-
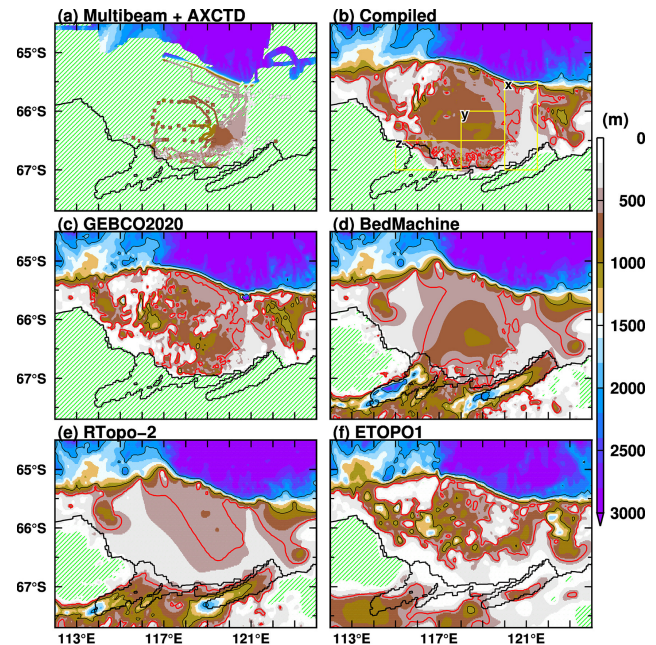

Figure A1. Comparison between water depth representations of bathymetric datasets: **(a)** direct observations from multibeam and airborne expendable CTD (AXCTD), **(b)** compiled data, **(c)** GEBCO2020, **(d)** BedMachine, **(e)** Rtopo-2, and **(f)** ETOPO1. The black lines in all the panels represent the grounding or ice front line in the model. The squares in panel **(a)** are the observed depth measurements from AXCTD; yellow rectangles with labels x, y, and z in panel **(b)** are the regions used in comparisons made in the main text. The red contours in panels **(b–f)** show a depth of 500 m to highlight the difference between the bottom topography of the datasets. Green-shaded areas represent uncharted areas in panel **(a)** and land grid points in the other panels.

Machine represent the deep depression, although the overall structure of the depression differs between the two. In RTopo-2 and ETOPO1, the depression is shallower than the observed depth. Finally, looking at the region in front of the TIS (region z), the observed deep trough (> 600 m) that connects the Sabrina Depression and the TIS cavity (Hirano et al., 2023) is only confirmed in BedMachine. The other three datasets show shallower structures toward the coast or ice front. The recently compiled bathymetry (Fig. A1b) reasonably captures the observed bathymetry in the Sabrina Depression. However, because the data do not include bathymetry below the ice shelf, we used BedMachine for the bathymetry in the ice shelf regions. In the region within 20 km from the ice front, which is treated as a transition zone, we selected a deeper depth between the two. We consider that our model topography is the best estimate when taking into account the direct bathymetric observations.

References

Adcroft, A., Hill, C., and Marshall, A. J.: Representation of topography by shaved cells in a height coordinate ocean model, Mon. Weather Rev., 125, 2293–2315, https://doi.org/10.1175/1520-0493(1997)125<2293:ROTBSC>2.0.CO;2, 1997.

Adusumilli, S., Fricker, H. A., Medley, B., Padman, L., and Siegfried, M. R.: Interannual variations in meltwater input to the Southern Ocean from Antarctic ice shelves, Nat. Geosci., 13, 616–620, https://doi.org/10.1038/s41561-020-0616-z, 2020.

Amante, C. and Eakins, B. W.: ETOPO1 1 Arc-Minute Global Relief Model: Procedures, Data Sources and Analysis, NOAA Technical Memorandum NESDIS NGDC-24, 19 pp., https://doi.org/10.1594/PANGAEA.769615, 2009.

Arndt, J. E., Schenke, H. W., Jakobsson, M., Nitsche, F. O., Buys, G., Goleby, B., Rebesco, M., Bohoyo, F., Hong, J., Black, J., Greku, R., Udintsev, G., Barrios, F., Reynoso-Peralta, W., Taisei, M., and Wigley, R.: The international bathymetric chart of the Southern Ocean (IBCSO) version 1.0-A new bathymetric compilation covering circum-Antarctic waters, Geophys. Res. Lett., 40, 3111–3117, https://doi.org/10.1002/grl.50413, 2013.

Assmann, K. M., Jenkins, A., Shoosmith, D. R., Walker, D. P., Jacobs, S. S., and Nicholls, K. W.: Variability of circumpolar deep water transport onto the Amundsen Sea Continental shelf through a shelf break trough, J. Geophys. Res.-Oceans, 118, 6603–6620, https://doi.org/10.1002/2013JC008871, 2013.

Bell, B., Hersbach, H., Simmons, A., Berrisford, P., Dahlgren, P., Horányi, A., Muñoz-Sabater, J., Nicolas, J., Radu, R., Schepers, D., Soci, C., Villaume, S., Bidlot, J. R., Haimberger, L., Woollen, J., Buontempo, C., and Thépaut, J. N.: The ERA5 global reanalysis: Preliminary extension to 1950, Q. J. Roy. Meteor. Soc., 147, 4186-4227, https://doi.org/10.1002/qj.4174, 2021.

Bindoff, N. L., Rosenberg, M. A., and Warner, M. J.: On the circulation of the waters over the Antarctic continental rise and slope between 80 and 150oE, Deep. Res. II, 47, 2299–2326, 2000.

Bracegirdle, T. J., Shuckburgh, E., Sallee, J. B., Wang, Z., Meijers, A. J. S., Bruneau, N., Phillips, T., and Wilcox, L. J.: Assessment of surface winds over the atlantic, indian, and pacific ocean sectors of the southern ocean in cmip5 models: Historical bias, forcing response, and state dependence, J. Geophys. Res.-Atmos., 118, 547–562, https://doi.org/10.1002/jgrd.50153, 2013.

Cavalieri, D. J., Gloersen, P., and Campbell, W. J.: Determination of sea ice parameters with the NIMBUS 7 SMMR, J. Geophys. Res.-Atmos., 89, 5355–5369, https://doi.org/10.1029/JD089iD04p05355, 1984.

Chavanne, C. P., Heywood, K. J., Nicholls, K. W., and Fer, I.: Observations of the Antarctic Slope undercurrent in the Southeastern Weddell Sea, Geophys. Res. Lett., 37, https://doi.org/10.1029/2010GL043603, 2010.

Dansereau, V., Heimbach, P., and Losch, M.: Simulation of subice shelf melt rates in a general circulation model: Velocity-dependent transfer and the role of friction, J. Geophys. Res.-Oceans, 119, 1765–1790, https://doi.org/10.1002/2013JC008846, 2014.

DeConto, R. M. and Pollard, D.: Contribution of Antarctica to past and future sea-level rise, Nature, 531, 591–597, https://doi.org/10.1038/nature17145, 2016.

Depoorter, M. A., Bamber, J. L., Griggs, J. A., Lenaerts, J. T. M., Ligtenberg, S. R. M., van den Broeke, M. R., and Moholdt, G.: Calving fluxes and basal melt rates of Antarctic ice shelves, Nature, 502, 89–92, https://doi.org/10.1038/nature12567, 2013.

DiGirolamo, N., Parkinson, C. L., Cavalieri, D. J., Gloersen, P., and Zwally, H. J.: Sea Ice Concentrations from Nimbus-7 SMMR and DMSP SSM/I-SSMIS Passive Microwave Data, Version 2, Boulder, Colorado USA, NASA National Snow and Ice Data Center Distributed Active Archive Center [data set], https://doi.org/10.5067/MPYG15WAA4WX, 2022.

Fraser, A. D., Massom, R. A., Michael, K. J., Galton-Fenzi, B. K., and Lieser, J. L.: East antarctic landfast sea ice distribution and variability, 2000–08, J. Climate, 25, 1137–1156, https://doi.org/10.1175/JCLI-D-10-05032.1, 2012.

Fraser, A. D., Massom, R. A., Handcock, M. S., Reid, P., Ohshima, K. I., Raphael, M. N., Cartwright, J., Klekociuk, A. R., Wang, Z., and Porter-Smith, R.: Eighteen-year record of circum-Antarctic landfast-sea-ice distribution allows detailed baseline characterisation and reveals trends and variability, The Cryosphere, 15, 5061–5077, https://doi.org/10.5194/tc-15-5061-2021, 2021.

Fretwell, P., Pritchard, H. D., Vaughan, D. G., Bamber, J. L., Barrand, N. E., Bell, R., Bianchi, C., Bingham, R. G., Blankenship, D. D., Casassa, G., Catania, G., Callens, D., Conway, H., Cook, A. J., Corr, H. F. J., Damaske, D., Damm, V., Ferraccioli, F., Forsberg, R., Fujita, S., Gim, Y., Gogineni, P., Griggs, J. A., Hindmarsh, R. C. A., Holmlund, P., Holt, J. W., Jacobel, R. W., Jenkins, A., Jokat, W., Jordan, T., King, E. C., Kohler, J., Krabill, W., Riger-Kusk, M., Langley, K. A., Leitchenkov, G., Leuschen, C., Luyendyk, B. P., Matsuoka, K., Mouginot, J., Nitsche, F. O., Nogi, Y., Nost, O. A., Popov, S. V., Rignot, E., Rippin, D. M., Rivera, A., Roberts, J., Ross, N., Siegert, M. J., Smith, A. M., Steinhage, D., Studinger, M., Sun, B., Tinto, B. K., Welch, B. C., Wilson, D., Young, D. A., Xiangbin, C., and Zirizzotti, A.: Bedmap2: improved ice bed, surface and thickness datasets for Antarctica, The Cryosphere, 7, 375–393, https://doi.org/10.5194/tc-7-375-2013, 2013.

GEBCO_2020 Grid: https://www.gebco.net/data_and_products/gridded_bathymetry_data/gebco_2020/ (last access: 22 May 2023), 2020.

Golledge, N. R., Kowalewski, D. E., Naish, T. R., Levy, R. H., Fogwill, C. J., and Gasson, E. G. W.: The multi-millennial Antarctic commitment to future sea-level rise, Nature, 526, 421–425, https://doi.org/10.1038/nature15706, 2015.

Gong, D. and Wang, S.: Definition of Antarctic oscillation index, Geophys. Res. Lett., 26, 459–462, https://doi.org/10.1029/1999GL900003, 1999.

Greenbaum, J. S., Blankenship, D. D., Young, D. A., Richter, T. G., Roberts, J. L., Aitken, A. R. A., Legresy, B., Schroeder, D. M., Warner, R. C., Van Ommen, T. D., and Siegert, M. J.: Ocean access to a cavity beneath Totten Glacier in East Antarctica, Nat. Geosci., 8, 294–298, https://doi.org/10.1038/ngeo2388, 2015.

Greene, C. A., Gardner, A. S., Schlegel, N. J., and Fraser, A. D.: Antarctic calving loss rivals ice-shelf thinning, Nature, 609, 948–953, https://doi.org/10.1038/s41586-022-05037-w, 2022.

Gwyther, D. E., Galton-Fenzi, B. K., Hunter, J. R., and Roberts, J. L.: Simulated melt rates for the Totten and Dalton ice shelves, Ocean Sci., 10, 267–279, https://doi.org/10.5194/os-10-267-2014, 2014.

Gwyther, D. E., O'Kane, T. J., Galton-Fenzi, B. K., Monselesan, D. P., and Greenbaum, J. S.: Intrinsic processes drive variability in basal melting of the Totten Glacier Ice Shelf, Nat. Commun., 9, 3141, https://doi.org/10.1038/s41467-018-05618-2, 2018.

Gwyther, D. E., Kusahara, K., Asay-Davis, X. S., Dinniman, M. S., and Galton-Fenzi, B. K.: Vertical processes and resolution impact ice shelf basal melting: A multi-model study, Ocean Model., 147, 101569, https://doi.org/10.1016/j.ocemod.2020.101569, 2020.

Hasumi, H.: CCSR Ocean Component Model (COCO) Version 4.0, http://ccsr.aori.u-tokyo.ac.jp/~hasumi/COCO/ (last access: 22 May 2023), 2006.

Hellmer, H. H. and Olbers, D. J.: A two-dimensional model for the thermohaline circulation under an ice shelf, Antarct. Sci., 1, 325–336, https://doi.org/10.1017/S0954102089000490, 1989.

Herraiz-Borreguero, L. and Naveira Garabato, A. C.: Poleward shift of Circumpolar Deep Water threatens the East Antarctic Ice Sheet, Nat. Clim. Change, 12, 728–734, https://doi.org/10.1038/s41558-022-01424-3, 2022.

Hersbach, H., Bell, B., Berrisford, P., Hirahara, S., Horányi, A., Muñoz-Sabater, J., Nicolas, J., Peubey, C., Radu, R., Schepers, D., Simmons, A., Soci, C., Abdalla, S., Abellan, X., Balsamo, G., Bechtold, P., Biavati, G., Bidlot, J., Bonavita, M., De Chiara, G., Dahlgren, P., Dee, D., Diamantakis, M., Dragani, R., Flemming, J., Forbes, R., Fuentes, M., Geer, A., Haimberger, L., Healy, S., Hogan, R. J., Hólm, E., Janisková, M., Keeley, S., Laloyaux, P., Lopez, P., Lupu, C., Radnoti, G., de Rosnay, P., Rozum, I., Vamborg, F., Villaume, S., and Thépaut, J. N.: The ERA5 global reanalysis, Q. J. Roy. Meteor. Soc., 146, 1999–2049, https://doi.org/10.1002/qj.3803, 2020.

Heywood, K. J., Locarnini, R. A., Frew, R. D., Dennis, P. F., and King, B. A.: Transport and Water Masses of the Antarctic Slope Front System in The Eastern Weddell Sea, in: Antarctic Research Series Ocean, Ice, and Atmosphere: Interactions at the Antarctic Continental Margin, edited by: Jacobs, S. S. and Weiss, R. F., American Geophysical Union, 203–214, https://doi.org/10.1029/ar075p0203, 1998.

Hirano, D., Mizobata, K., Sasaki, H., Murase, H., Tamura, T., and Aoki, S.: Poleward eddy-induced warm water transport across a shelf break off Totten Ice Shelf, East Antarctica, Commun. Earth Environ., 2, 153, https://doi.org/10.1038/s43247-021-00217-4, 2021.

Hirano, D., Tamura, T., Kusahara, K., Fujii, M., Rintoul, S. R., Yamazaki, K., Nakayama, Y., Ono, K., Itaki, T., Aoyama, Y., Simizu, D., Mizobata, K., Ohshima, K. I., Nogi, Y., van Wijk, E., Greenbaum, J. S., Blankenship, D. D., Saito, K., and Aoki, S.: On-shelf circulation of warm water toward the Totten Ice Shelf in East Antarctica, Nat. Commun., 14, 4955, https://doi.org/10.1038/s41467-023-39764-z, 2023.

Holland, D. M. and Jenkins, A.: Modeling thermodynamic ice–ocean interactions at the base of an ice shelf, J.

Phys. Oceanogr., 29, 1787–1800, https://doi.org/10.1175/1520-0485(1999)029<1787:MTIOIA>2.0.CO;2, 1999.

IPCC: Climate Change 2021: The Physical Science Basis. Contribution of Working Group I to the Sixth Assessment Report of the Intergovernmental Panel on Climate Change, Cambridge Univ. Press, ISBN-10 1009157884, ISBN-13 978-1009157889, 2021.

Kara, A. B., Rochford, P. A., and Hurlburt, H. E.: Efficient and accurate bulk parameterizations of air–sea fluxes for use in general circulation models, J. Atmos. Ocean. Tech., 17, 1421–1438, https://doi.org/10.1175/1520-0426(2000)017<1421:EAABPO>2.0.CO;2, 2000.

Khazendar, A., Schodlok, M. P., Fenty, I., Ligtenberg, S. R. M., Rignot, E., and Van Den Broeke, M. R.: Observed thinning of Totten Glacier is linked to coastal polynya variability, Nat. Commun., 4, 2857, https://doi.org/10.1038/ncomms3857, 2013.

Kimura, S., Jenkins, A., Regan, H., Holland, P. R., Assmann, K. M., Whitt, D. B., Van Wessem, M., van de Berg, W. J., Reijmer, C. H., and Dutrieux, P.: Oceanographic Controls on the Variability of Ice-Shelf Basal Melting and Circulation of Glacial Meltwater in the Amundsen Sea Embayment, Antarctica, J. Geophys. Res.-Oceans, 122, 10131–10155, https://doi.org/10.1002/2017JC012926, 2017.

Kusahara, K.: Summertime linkage between Antarctic sea-ice extent and ice-shelf basal melting through Antarctic coastal water masses' variability: A circumpolar Southern Ocean model study, Environ. Res. Lett., 16, 074042, https://doi.org/10.1088/1748-9326/ac0de0, 2021.

Kusahara, K. and Hasumi, H.: Modeling Antarctic ice shelf responses to future climate changes and impacts on the ocean, J. Geophys. Res.-Oceans, 118, 2454–2475, https://doi.org/10.1002/jgrc.20166, 2013.

Kusahara, K. and Hasumi, H.: Pathways of basal meltwater from Antarctic ice shelves: A model study, J. Geophys. Res.-Oceans, 119, 5690–5704, https://doi.org/10.1002/2014JC009915, 2014.

Kusahara, K., Hasumi, H., Fraser, A. D., Aoki, S., Shimada, K., Williams, G. D., Massom, R., and Tamura, T.: Modeling ocean-cryosphere interactions off adélie and George V Land, East Antarctica, J. Climate, 30, 163–188, https://doi.org/10.1175/JCLI-D-15-0808.1, 2017.

Kusahara, K., Hirano, D., Fujii, M., Fraser, A. D., and Tamura, T.: Modeling intensive ocean–cryosphere interactions in Lützow-Holm Bay, East Antarctica, The Cryosphere, 15, 1697–1717, https://doi.org/10.5194/tc-15-1697-2021, 2021.

Kusahara, K., Hirano, D., Fujii, M., Fraser, A., Tamura, T., Mizobata, K., Williams, G., and Aoki, S.: Data for "Modeling seasonal-to-decadal ocean-cryosphere interactions along the Sabrina Coast, East Antarctica", V1, Mendeley Data [data set], https://doi.org/10.17632/zf6h9pvxd8.1, 2023.

Li, R., Cheng, Y., Chang, T., Gwyther, D. E., Forbes, M., An, L., Xia, M., Yuan, X., Qiao, G., Tong, X., and Ye, W.: Satellite record reveals 1960s acceleration of Totten Ice Shelf in East Antarctica, Nat. Commun., 14, 4061, https://doi.org/10.1038/s41467-023-39588-x, 2023.

Li, X., Rignot, E., Morlighem, M., Mouginot, J., and Scheuchl, B.: Grounding line retreat of Totten Glacier, East Antarctica, 1996 to 2013, Geophys. Res. Lett., 42, 8049–8056, https://doi.org/10.1002/2015GL065701, 2015.

Li, X., Rignot, E., Mouginot, J., and Scheuchl, B.: Ice flow dynamics and mass loss of Totten Glacier, East Antarctica,

from 1989 to 2015, Geophys. Res. Lett., 43, 6366–6373, https://doi.org/10.1002/2016GL069173, 2016.

Liu, C., Wang, Z., Liang, X., Li, X., Li, X., Cheng, C., and Qi, D.: Topography-mediated Transport of Warm Deep Water across the Continental Shelf Slope, East Antarctica, J. Phys. Oceanogr., 52, 1295–1314, https://doi.org/10.1175/jpo-d-22-0023.1, 2022.

Liu, Y., Liang, X. S., and Weisberg, R. H.: Rectification of the bias in the wavelet power spectrum, J. Atmos. Ocean. Tech., 24, 2093–2102, https://doi.org/10.1175/2007JTECHO511.1, 2007.

Liu, Y., Moore, J. C., Cheng, X., Gladstone, R. M., Bassis, J. N., Liu, H., Wen, J., and Hui, F.: Ocean-driven thinning enhances iceberg calving and retreat of Antarctic ice shelves, P. Natl. Acad. Sci. USA, 112, 3263–3268, https://doi.org/10.1073/pnas.1415137112, 2015.

Locarnini, R. A., Mishonov, A. V., Baranova, O. K., Boyer, T. P., Zweng, M. M., Garcia, H. E., Reagan, J. R., Seidov, D., Weathers, K. W., Paver, C. R., and Smolyar, I. V.: World Ocean Atlas 2018, Vol. 1: Temperature, NOAA Atlas NESDIS 81, https://www.ncei.noaa.gov/access/world-ocean-atlas-2018/ (last access: 22 May 2023), 2018.

Malyarenko, A., Wells, A. J., Langhorne, P. J., Robinson, N. J., Williams, M. J. M., and Nicholls, K. W.: A synthesis of thermodynamic ablation at ice–ocean interfaces from theory, observations and models, Ocean Model., 154, 101692, https://doi.org/10.1016/j.ocemod.2020.101692, 2020.

Marshall, J. and Speer, K.: Closure of the meridional overturning circulation through Southern Ocean upwelling, Nat. Geosci., 5, 171–180, https://doi.org/10.1038/ngeo1391, 2012.

Marsland, S. J., Bindoff, N. L., Williams, G. D., and Budd, W. F.: Modeling water mass formation in the Mertz Glacier Polynya and Adélie Depression, East Antarctica, J. Geophys. Res., 109, C11003, https://doi.org/10.1029/2004JC002441, 2004.

McCormack, F. S., Roberts, J. L., Gwyther, D. E., Morlighem, M., Pelle, T., and Galton-Fenzi, B. K.: The Impact of Variable Ocean Temperatures on Totten Glacier Stability and Discharge, Geophys. Res. Lett., 48, e2020GL091790, https://doi.org/10.1029/2020GL091790, 2021.

Miles, B. W. J., Stokes, C. R., Jamieson, S. S. R., Jordan, J. R., Gudmundsson, G. H., and Jenkins, A.: High spatial and temporal variability in Antarctic ice discharge linked to ice shelf buttressing and bed geometry, Sci. Rep.-UK, 12, 10968, https://doi.org/10.1038/s41598-022-13517-2, 2022.

Milillo, P., Rignot, E., Rizzoli, P., Scheuchl, B., Mouginot, J., Bueso-Bello, J., and Prats-Iraola, P.: Heterogeneous retreat and ice melt of thwaites glacier, West Antarctica, Sci. Adv., 5, eaau3433, https://doi.org/10.1126/sciadv.aau3433, 2019.

Mimura, N.: Sea-level rise caused by climate change and its implications for society, P. Jpn. Acad. B-Phys., 89, 281–301, https://doi.org/10.2183/pjab.89.281, 2013.

Mizobata, K., Shimada, K., Aoki, S., and Kitade, Y.: The Cyclonic Eddy Train in the Indian Ocean Sector of the Southern Ocean as Revealed by Satellite Radar Altimeters and In Situ Measurements, J. Geophys. Res.-Oceans, 125, e2019JC015994, https://doi.org/10.1029/2019JC015994, 2020.

Morales Maqueda, M. A., Willmott, A. J., and Biggs, N. R. T.: Polynya Dynamics: A review of observations and modeling, Rev. Geophys., 42, RG1004, https://doi.org/10.1029/2002RG000116, 2004.

Morlighem, M.: MEaSUREs BedMachine Antarctica, Version 2, Boulder, Colorado USA, NASA National Snow and Ice Data Center Distributed Active Archive Center [data set], https://doi.org/10.5067/E1QL9HFQ7A8M, 2020.

Morlighem, M., Rignot, E., Binder, T., Blankenship, D., Drews, R., Eagles, G., Eisen, O., Ferraccioli, F., Forsberg, R., Fretwell, P., Goel, V., Greenbaum, J. S., Gudmundsson, H., Guo, J., Helm, V., Hofstede, C., Howat, I., Humbert, A., Jokat, W., Karlsson, N. B., Lee, W. S., Matsuoka, K., Millan, R., Mouginot, J., Paden, J., Pattyn, F., Roberts, J., Rosier, S., Ruppel, A., Seroussi, H., Smith, E. C., Steinhage, D., Sun, B., van den Broeke, M. R., van Ommen, T. D., van Wessem, M., and Young, D. A.: Deep glacial troughs and stabilizing ridges unveiled beneath the margins of the Antarctic ice sheet, Nat. Geosci., 13, 132–137, https://doi.org/10.1038/s41561-019-0510-8, 2020.

Mueller, R. D., Padman, L., Dinniman, M. S., Erofeeva, S. Y., Fricker, H. A., and King, M. A.: Impact of tide-topography interactions on basal melting of Larsen C Ice Shelf, Antarctica, J. Geophys. Res.-Oceans, 117, C05005, https://doi.org/10.1029/2011JC007263, 2012.

Nakata, K., Ohshima, K. I., and Nihashi, S.: Mapping of Active Frazil for Antarctic Coastal Polynyas, With an Estimation of Sea-Ice Production, Geophys. Res. Lett., 48, e2020GL091353, https://doi.org/10.1029/2020GL091353, 2021.

Nakayama, Y., Greene, C. A., Paolo, F. S., Mensah, V., Zhang, H., Kashiwase, H., Simizu, D., Greenbaum, J. S., Blankenship, D. D., Abe-Ouchi, A., and Aoki, S.: Antarctic Slope Current Modulates Ocean Heat Intrusions Towards Totten Glacier, Geophys. Res. Lett., 48, e2021GL094149, https://doi.org/10.1029/2021GL094149, 2021.

Naughten, K. A., Holland, P. R., Dutrieux, P., Kimura, S., Bett, D. T., and Jenkins, A.: Simulated Twentieth-Century Ocean Warming in the Amundsen Sea, West Antarctica, Geophys. Res. Lett., 49, e2021GL094566, https://doi.org/10.1029/2021GL094566, 2022.

Neme, J., England, M. H., and Hogg, A. McC.: Projected Changes of Surface Winds Over the Antarctic Continental Margin, Geophys. Res. Lett., 49, e2022GL098820, https://doi.org/10.1029/2022GL098820, 2022.

Nihashi, S. and Ohshima, K. I.: Circumpolar mapping of Antarctic coastal polynyas and landfast sea ice: relationship and variability, J. Climate, 28, 3650–3670, https://doi.org/10.1175/JCLI-D-14-00369.1, 2015.

Nitsche, F. O., Porter, D., Williams, G., Cougnon, E. A., Fraser, A. D., Correia, R., and Guerrero, R.: Bathymetric control of warm ocean water access along the East Antarctic Margin, Geophys. Res. Lett., 44, 8936–8944, https://doi.org/10.1002/2017GL074433, 2017.

NOAA National Centers for Environmental Information: ETOPO 2022 15 Arc-Second Global Relief Model, NOAA National Centers for Environmental Information [data set], https://doi.org/10.25921/fd45-gt74, 2022.

Núñez-Riboni, I. and Fahrbach, E.: Seasonal variability of the Antarctic Coastal Current and its driving mechanisms in the Weddell Sea, Deep-Sea Res. Pt. I, 56, 1927–1941, https://doi.org/10.1016/j.dsr.2009.06.005, 2009.

Orsi, A. H. and Webb, C. J.: Impact of Sea Ice Production off Sabrina Coast, East Antarctica, Geophys. Res. Lett., 49, e2021GL095613, https://doi.org/10.1029/2021GL095613, 2022.

Otosaka, I. N., Shepherd, A., Ivins, E. R., Schlegel, N.-J., Amory, C., van den Broeke, M. R., Horwath, M., Joughin, I., King, M. D., Krinner, G., Nowicki, S., Payne, A. J., Rignot, E., Scambos, T., Simon, K. M., Smith, B. E., Sørensen, L. S., Velicogna, I., Whitehouse, P. L., A, G., Agosta, C., Ahlstrøm, A. P., Blazquez, A., Colgan, W., Engdahl, M. E., Fettweis, X., Forsberg, R., Gallée, H., Gardner, A., Gilbert, L., Gourmelen, N., Groh, A., Gunter, B. C., Harig, C., Helm, V., Khan, S. A., Kittel, C., Konrad, H., Langen, P. L., Lecavalier, B. S., Liang, C.-C., Loomis, B. D., McMillan, M., Melini, D., Mernild, S. H., Mottram, R., Mouginot, J., Nilsson, J., Noël, B., Pattle, M. E., Peltier, W. R., Pie, N., Roca, M., Sasgen, I., Save, H. V., Seo, K.-W., Scheuchl, B., Schrama, E. J. O., Schröder, L., Simonsen, S. B., Slater, T., Spada, G., Sutterley, T. C., Vishwakarma, B. D., van Wessem, J. M., Wiese, D., van der Wal, W., and Wouters, B.: Mass balance of the Greenland and Antarctic ice sheets from 1992 to 2020, Earth Syst. Sci. Data, 15, 1597–1616, https://doi.org/10.5194/essd-15-1597-2023, 2023.

Payne, A. J., Vieli, A., Shepherd, A. P., Wingham, D. J., and Rignot, E.: Recent dramatic thinning of largest West Antarctic ice stream triggered by oceans, Geophys. Res. Lett., 31, 1–4, https://doi.org/10.1029/2004GL021284, 2004.

Pelle, T., Morlighem, M., and McCormack, F. S.: Aurora Basin, the Weak Underbelly of East Antarctica, Geophys. Res. Lett., 47, e2019GL086821, https://doi.org/10.1029/2019GL086821, 2020.

Pelle, T., Morlighem, M., Nakayama, Y., and Seroussi, H.: Widespread Grounding Line Retreat of Totten Glacier, East Antarctica, Over the 21st Century, Geophys. Res. Lett., 48, e2021GL093213, https://doi.org/10.1029/2021GL093213, 2021.

Peña-Molino, B., McCartney, M. S., and Rintoul, S. R.: Direct observations of the Antarctic Slope Current transport at 113° E, J. Geophys. Res.-Oceans, 121, 7390–7407, https://doi.org/10.1002/2015JC011594, 2016.

Pollard, D., DeConto, R. M., and Alley, R. B.: Potential Antarctic Ice Sheet retreat driven by hydrofracturing and ice cliff failure, Earth Planet. Sc. Lett., 412, 112–121, https://doi.org/10.1016/j.epsl.2014.12.035, 2015.

Pritchard, H. D., Ligtenberg, S. R. M., Fricker, H. A., Vaughan, D. G., van den Broeke, M. R., and Padman, L.: Antarctic ice-sheet loss driven by basal melting of ice shelves, Nature, 484, 502–505, https://doi.org/10.1038/nature10968, 2012.

Rignot, E., Bamber, J. L., van den Broeke, M. R., Davis, C., Li, Y., van de Berg, W. J., and van Meijgaard, E.: Recent Antarctic ice mass loss from radar interferometry and regional climate modelling, Nat. Geosci., 1, 106–110, https://doi.org/10.1038/ngeo102, 2008.

Rignot, E., Jacobs, S., Mouginot, J., and Scheuchl, B.: Ice-shelf melting around Antarctica, Science, 341, 266–270, https://doi.org/10.1126/science.1235798, 2013.

Rignot, E., Mouginot, J., Scheuchl, B., Van Den Broeke, M., Van Wessem, M. J., and Morlighem, M.: Four decades of Antarctic ice sheet mass balance from 1979–2017, P. Natl. Acad. Sci. USA, 116, 1095–1103, https://doi.org/10.1073/pnas.1812883116, 2019.

Rintoul, S. R., Silvano, A., Pena-Molino, B., van Wijk, E., Rosenberg, M., Greenbaum, J. S., and Blankenship, D. D.: Ocean heat drives rapid basal melt of the Totten Ice Shelf, Sci. Adv., 2, e160161, https://doi.org/10.1126/sciadv.1601610, 2016.

Roberts, J., Galton-Fenzi, B. K., Paolo, F. S., Donnelly, C., Gwyther, D. E., Padman, L., Young, D., Warner, R., Greenbaum, J., Fricker, H. A., Payne, A. J., Cornford, S., Le Brocq, A., Van Ommen, T., Blankenship, D., and Siegert, M. J.: Ocean forced variability of Totten Glacier mass loss, Geol. Soc. Spec. Publ., 461, 175–186, https://doi.org/10.1144/SP461.6, 2018.

Schaffer, J. and Timmermann, R.: Greenland and Antarctic ice sheet topography, cavity geometry, and global bathymetry (RTopo-2), links to NetCDF files, PANGAEA [data set], https://doi.org/10.1594/PANGAEA.856844, 2016.

Schaffer, J., Timmermann, R., Arndt, J. E., Kristensen, S. S., Mayer, C., Morlighem, M., and Steinhage, D.: A global, high-resolution data set of ice sheet topography, cavity geometry, and ocean bathymetry, Earth Syst. Sci. Data, 8, 543–557, https://doi.org/10.5194/essd-8-543-2016, 2016.

Sergienko, O. V.: No general stability conditions for marine ice-sheet grounding lines in the presence of feedbacks, Nat. Commun., 13, 2265, https://doi.org/10.1038/s41467-022-29892-3, 2022.

Shepherd, A., Wingham, D., and Rignot, E.: Warm ocean is eroding West Antarctic Ice Sheet, Geophys. Res. Lett., 31, 1–4, https://doi.org/10.1029/2004GL021106, 2004.

Shepherd, A., Ivins, E. R., A, G., Barletta, V. R., Bentley, M. J., Bettadpur, S., Briggs, K. H., Bromwich, D. H., Forsberg, R., Galin, N., Horwath, M., Jacobs, S., Joughin, I., King, M. A., Lenaerts, J. T. M., Li, J., Ligtenberg, S. R. M., Luckman, A., Luthcke, S. B., McMillan, M., Meister, R., Milne, G., Mouginot, J., Muir, A., Nicolas, J. P., Paden, J., Payne, A. J., Pritchard, H., Rignot, E., Rott, H., Sandberg Sørensen, L., Scambos, T. A., Scheuchl, B., Schrama, E. J. O., Smith, B., Sundal, A. V., Angelen, V., Jan, H., De Berg, V., Willem, J., Den Broeke, V., Michiel, R., Vaughan, D. G., Velicogna, I., Wahr, J., Whitehouse, P., Wingham, D. J., Yi, D., Young, D., and Zwally, H. J.: A reconciled estimate of ice sheet mass balance, Science, 338, 1183–1189, https://doi.org/10.1126/science.1228102, 2012.

Shepherd, A., Ivins, E., Rignot, E., Smith, B., Van Den Broeke, M., Velicogna, I., Whitehouse, P., Briggs, K., Joughin, I., Krinner, G., Nowicki, S., Payne, T., Scambos, T., Schlegel, N., Geruo, A., Agosta, C., Ahlstrøm, A., Babonis, G., Barletta, V., Blazquez, A., Bonin, J., Csatho, B., Cullather, R., Felikson, D., Fettweis, X., Forsberg, R., Gallee, H., Gardner, A., Gilbert, L., Groh, A., Gunter, B., Hanna, E., Harig, C., Helm, V., Horvath, A., Horwath, M., Khan, S., Kjeldsen, K. K., Konrad, H., Langen, P., Lecavalier, B., Loomis, B., Luthcke, S., McMillan, M., Melini, D., Mernild, S., Mohajerani, Y., Moore, P., Mouginot, J., Moyano, G., Muir, A., Nagler, T., Nield, G., Nilsson, J., Noel, B., Otosaka, I., Pattle, M. E., Peltier, W. R., Pie, N., Rietbroek, R., Rott, H., Sandberg-Sørensen, L., Sasgen, I., Save, H., Scheuchl, B., Schrama, E., Schröder, L., Seo, K. W., Simonsen, S., Slater, T., Spada, G., Sutterley, T., Talpe, M., Tarasov, L., Van De Berg, W. J., Van Der Wal, W., Van Wessem, M., Vishwakarma, B. D., Wiese, D., and Wouters, B.: Mass balance of the Antarctic Ice Sheet from 1992 to 2017, Nature, 558, 219–222, https://doi.org/10.1038/s41586-018-0179-y, 2018.

Silvano, A., Rintoul, S. R., Peña-Molino, B., and Williams, G. D.: Distribution of water masses and meltwater on the continental shelf near the Totten and Moscow University ice shelves, J. Geophys. Res.-Oceans, 122, 2050–2068, https://doi.org/10.1002/2016JC012115, 2017.

Silvano, A., Rintoul, S. R., Kusahara, K., Peña-Molino, B., van Wijk, E., Gwyther, D. E., and Williams, G. D.: Seasonality of Warm Water Intrusions Onto the Continental Shelf Near the Totten Glacier, J. Geophys. Res.-Oceans, 124, 4272–4289, https://doi.org/10.1029/2018JC014634, 2019.

Silvano, A., Holland, P. R., Naughten, K. A., Dragomir, O., Dutrieux, P., Jenkins, A., Si, Y., Stewart, A. L., Peña Molino, B., Janzing, G. W., Dotto, T. S., and Naveira Garabato, A. C.: Baroclinic Ocean Response to Climate Forcing Regulates Decadal Variability of Ice-Shelf Melting in the Amundsen Sea, Geophys. Res. Lett., 49, e2022GL100646, https://doi.org/10.1029/2022GL100646, 2022.

Smedsrud, L. H., Jenkins, A., Holland, D. M., and Nøst, O. A.: Modeling ocean processes below Fimbulisen, Antarctica, J. Geophys. Res.-Oceans, 111, C01107, https://doi.org/10.1029/2005JC002915, 2006.

Sun, C., Liu, C., Wang, Z., Yan, L., Tao, Y., Qin, Q., and Qian, J.: On the influences of the continental shelf bathymetry correction in Prydz Bay, East Antarctica, Front. Mar. Sci., 9, 957414, https://doi.org/10.3389/fmars.2022.957414, 2022.

Sun, S., Cornford, S. L., Gwyther, D. E., Gladstone, R. M., Galton-Fenzi, B. K., Zhao, L., and Moore, J. C.: Impact of ocean forcing on the Aurora Basin in the 21st and 22nd centuries, Ann. Glaciol., 57, 79–86, https://doi.org/10.1017/aog.2016.27, 2016.

Swift, C. T. and Cavalieri, D. J.: Passive microwave remote sensing for sea ice research, Eos T. Am. Geophys. Un., 66, 1210–1212, https://doi.org/10.1029/EO066i049p01210, 1985.

Tamsitt, V., Drake, H. F., Morrison, A. K., Talley, L. D., Dufour, C. O., Gray, A. R., Griffies, S. M., Mazloff, M. R., Sarmiento, J. L., Wang, J., and Weijer, W.: Spiraling pathways of global deep waters to the surface of the Southern Ocean, Nat. Commun., 8, 172, https://doi.org/10.1038/s41467-017-00197-0, 2017.

Tamura, T., Ohshima, K. I., and Nihashi, S.: Mapping of sea ice production for Antarctic coastal polynyas, Geophys. Res. Lett., 35, L07606, https://doi.org/10.1029/2007GL032903, 2008.

Tamura, T., Ohshima, K. I., Fraser, A. D., and Williams, G. D.: Sea ice production variability in Antarctic coastal polynyas, J. Geophys. Res., 121, 2967–2979, https://doi.org/10.1002/2015JC011486, 2016.

Thompson, A. F., Stewart, A. L., Spence, P., and Heywood, K. J.: The Antarctic Slope Current in a Changing Climate, Rev. Geophys., 56, 741–770, https://doi.org/10.1029/2018RG000624, 2018.

Torrence, C. and Compo, G. P.: A Practical Guide to Wavelet Analysis, B. Am. Meteorol. Soc., 79, 61–78, https://doi.org/10.1175/1520-0477(1998)079< 0061:APGTWA> 2.0.CO;2, 1998.

Van Achter, G., Fichefet, T., Goosse, H., Pelletier, C., Sterlin, J., Huot, P. V., Lemieux, J. F., Fraser, A. D., Haubner, K., and Porter-Smith, R.: Modelling landfast sea ice and its influence on ocean–ice interactions in the area of the Totten Glacier, East Antarctica, Ocean Model., 169, 101920, https://doi.org/10.1016/j.ocemod.2021.101920, 2022.

Vaňková, I., Cook, S., Winberry, J. P., Nicholls, K. W., and Galton-Fenzi, B. K.: Deriving Melt Rates at a Complex Ice Shelf Base Using In Situ Radar: Application to Totten Ice Shelf, Geophys. Res. Lett., 48, e2021GL092692, https://doi.org/10.1029/2021GL092692, 2021.

Vaňková, I., Winberry, J. P., Cook, S., Nicholls, K. W., Greene, C. A., and Galton-Fenzi, B. K.: High Spatial Melt Rate Variability Near the Totten Glacier Grounding Zone Explained by New Bathymetry Inversion, Geophys. Res. Lett., 50, e2023GL102960, https://doi.org/10.1029/2023GL102960, 2023.

Wakatsuchi, M., Ohshima, K. I., Hishida, M., and Naganobu, M.: Observations of a street of cyclonic eddies in the Indian Ocean sector of the Antarctic Divergence, J. Geophys. Res., 99, 20417–20426, https://doi.org/10.1029/94jc01478, 1994.

Walker, D. P., Jenkins, A., Assmann, K. M., Shoosmith, D. R., and Brandon, M. A.: Oceanographic observations at the shelf break of the Amundsen Sea, Antarctica, J. Geophys. Res.-Oceans, 118, 2906–2918, https://doi.org/10.1002/jgrc.20212, 2013.

Weertman, J.: Stability of the Junction of an Ice Sheet and an Ice Shelf, J. Glaciol., 13, 3–11, https://doi.org/10.3189/s0022143000023327, 1974.

Williams, G. D., Meijers, A. J. S., Poole, A., Mathiot, P., Tamura, T., and Klocker, A.: Late winter oceanography off the Sabrina and BANZARE coast (117–128° E), East Antarctica, Deep-Sea Res. Pt. II, 58, 1194–1210, https://doi.org/10.1016/j.dsr2.2010.10.035, 2011.

Yamazaki, K., Aoki, S., Katsumata, K., Hirano, D., and Nakayama, Y.: Multidecadal poleward shift of the southern boundary of the Antarctic Circumpolar Current off East Antarctica, Sci. Adv., 7, eabf8755, https://doi.org/10.1126/sciadv.abf8755, 2021.

Young, D. A., Wright, A. P., Roberts, J. L., Warner, R. C., Young, N. W., Greenbaum, J. S., Schroeder, D. M., Holt, J. W., Sugden, D. E., Blankenship, D. D., Van Ommen, T. D., and Siegert, M. J.: A dynamic early East Antarctic Ice Sheet suggested by ice-covered fjord landscapes, Nature, 474, 72–75, https://doi.org/10.1038/nature10114, 2011.

Zheng, F., Li, J., Clark, R. T., and Nnamchi, H. C.: Simulation and projection of the Southern Hemisphere annular mode in CMIP5 models, J. Climate, 26, 9860–9879, https://doi.org/10.1175/JCLI-D-13-00204.1, 2013.

Zweng, M. M., Reagan, J. R., Seidov, D., Boyer, T. P., Antonov, J. I., Locarnini, R. A., Garcia, H. E., Mishonov, A. V., Baranova, O. K., Weathers, K. W., Paver, C. R., and Smolyar, I. V.: World Ocean Atlas 2018, Vol. 2: Salinity, NOAA Atlas NESDIS, https://www.ncei.noaa.gov/access/world-ocean-atlas-2018/ (last access: 22 May 2023), 2019.